Development of crystallographic preferred orientation and microstructure during plastic deformation of natural coarse-grained quartz veins

Development of crystallographic preferred orientation and microstructure during plastic deformation of natural coarse-grained quartz veins

Giorgio Pennacchioni,[1] Luca Menegon,[2] Bernd Leiss,[3] Fabrizio Nestola,[1] and Geoffrey Bromiley[4]

Received 27 April 2010; revised 13 July 2010; accepted 2 August 2010; published 2 December 2010.

[1] The microstructure and crystallographic preferred orientation (CPO) of quartz were quantified in 17 samples of natural monomineralic tabular veins. The veins opened and were deformed, up to shear strain $\gamma > 15$, in a small temperature window (about 25°C) above 500°C, as established by Ti-in-quartz thermometry. The veins filled a set of fractures within the Adamello tonalite (southern Alps, Italy) and localized homogeneous simple shear during postmagmatic cooling. The local (square millimeter scale) and bulk (square centimeter) CPO were investigated by computer-integrated polarization microscopy (CIP) and X-ray texture goniometry. Weakly deformed veins (WDV: $\gamma < 1$) consist of millimeter- to centimeter-sized crystals with a strong CPO showing a *c*-axis girdle slightly inclined, mostly with the shear sense, to the foliation (XY) plane and a strong maximum close to the lineation (X). Moderately deformed veins (MDV: $2 < \gamma < 3$) consist of elongated nonrecrystallized ribbon grains and most have a CPO showing a strong Y maximum of *c* axes some with weak extension into a YZ girdle. Strongly deformed veins (SDV: $\gamma = 4$ to 15) are pervasively to completely recrystallized to fine (34–40 μm grain size) aggregates with a strong CPO similar to that of MDV. The slip systems during plastic deformation were dominantly prism ⟨a⟩ with subordinate rhomb and basal ⟨a⟩ slip. Recrystallization occurred rather abruptly for $3 < \gamma < 4$. In contrast to dislocation creep experiments in quartz (and other minerals), a steady-state recrystallized fabric is achieved at early stages of deformation ($\gamma \approx 4$) as there is no evidence, with increasing strain, of strengthening of the CPO, of rotation of the fabric skeleton, or of change in grain size. WDV represent weakly deformed relicts of veins with an initial CPO believed to have developed during crystal growth but unsuitably oriented for prism ⟨a⟩ slip during subsequent shear. MDV and SDV appear to derive from veins different from WDV, where the vein crystals grew with orientation favorable for prism ⟨a⟩ slip. The relationship between the initial growth CPO and the kinematic framework suggests that veins opened at a temperature close to that at which there is a switch between the activity of prism ⟨c⟩ and prism ⟨a⟩ slip, with the temperature of growth causing growth of crystals well oriented for slip. The initial CPO of veins, from which quartz mylonites are commonly derived, plays a critical role in the fabric evolution. The strong growth- and strain-induced CPOs of these sheared veins inhibited significant reworking during lower temperature stages of pluton cooling when basal ⟨a⟩ slip would have been dominant.

Citation: Pennacchioni, G., L. Menegon, B. Leiss, F. Nestola, and G. Bromiley (2010), Development of crystallographic preferred orientation and microstructure during plastic deformation of natural coarse-grained quartz veins, *J. Geophys. Res.*, *115*, B12405, doi:10.1029/2010JB007674.

[1]Dipartimento di Geoscienze, University of Padova, Padova, Italy.
[2]Institutt for geologi, Universitetet i Tromsø, Tromsø, Norway.
[3]Geowissenschaftliches Zentrum, Universität Göttingen (GZG), Göttingen, Germany.
[4]School of GeoSciences, University of Edinburgh, Grant Institute, Edinburgh, United Kingdom.

0148-0227/10/2010JB007674

1. Introduction

[2] High-temperature ductile deformation is often localized, at all scales, in approximately tabular zones of high strain (mylonitic shear zones) where simple shear, or noncoaxial deformation, is dominant [*Ramsay*, 1980]. Major high-strain zones typically accommodate a significant component of the total tectonic displacement. An under-

standing of shear zone nucleation and of strain localization mechanisms is therefore of paramount importance in modelling lithosphere dynamics. In the upper and middle continental crust, shear zones are commonly developed within quartz-dominated rocks and it is commonly assumed that the rheology of quartz is representative of crustal rheology [e.g., *Toussaint et al.*, 2004; *Regenauer-Lieb et al.*, 2006]. As a result, there are many experimental studies on the deformation of quartz and quartzite at high temperature, which have provided constitutive flow laws for steady-state dislocation creep [e.g., *Paterson and Luan*, 1990; *Gleason and Tullis*, 1995; *Brodie and Rutter*, 2000; *Rutter and Brodie*, 2004]. In such experiments, it is possible to integrate the mechanical data with textural (crystallographic preferred orientation (CPO)) and microstructural observations relative to specific amounts of accumulated strain. Therefore, the effect of fabric evolution (microstructure and CPO) on material strength can be evaluated. The interpretation of rock rheology at depth in the Earth is based on extrapolation of flow laws determined in the lab ($\dot{\varepsilon} \geq 10^{-6}$ s^{-1}) to geological strain rates ($\dot{\varepsilon} = 10^{-12} - 10^{-16}$ s^{-1}), assuming that the similarity between microstructures and CPOs in experimental and natural quartz mylonites reflects activity of the same deformation mechanisms [e.g. *Hirth et al.*, 2001; *Mancktelow and Pennacchioni*, 2010]. *Hirth and Tullis* [1992] defined, on an experimental basis, three dislocation creep regimes for quartz. *Stipp et al.* [2002] suggested that the calibration of the different CPOs and microstructures, along a temperature gradient in the metamorphic contact aureole of the Adamello pluton that was sheared during metamorphism, provides a potential reference scheme allowing one to use quartzite fabrics as a gauge to infer deformation temperatures.

[3] The assumption that the CPO depends mainly on the dominant intracrystalline slip systems [*Lister and Paterson*, 1979; *Schmid and Casey*, 1986] and that these are in turn dominantly controlled by the temperature of deformation (with the progressive activation of basal ⟨a⟩, rhomb ⟨a⟩, prism ⟨a⟩, and, finally, prism ⟨c⟩) is generally accepted. However, a compilation of literature data of the inferred slip systems as a function of temperature reveals remarkable inconsistencies [e.g., see Figure 8 of *Toy et al.*, 2008]. In addition, recent experiments on quartz [e.g., *Heilbronner and Tullis*, 2006], as well on other geologically relevant minerals, also show a clear dependence of the CPO on strain, as explained below.

[4] The comparison between fabrics of experimentally and naturally deformed quartzites, as well as between different quartz mylonites, is not simple. One reason is that the CPO and the microstructure of natural mylonites cannot generally be correlated to measured strain. In some cases the quartz fabric has been studied across strain gradients in heterogeneous shear zones within granitoid rocks and schists, which allowed an estimate of γ on the basis of the angle between foliation and the shear zone boundary [e.g., *Hara et al.*, 1973; *Burg and Laurent*, 1978; *van Roermund et al.*, 1979; *Carreras and Garcia Celma*, 1982; *Simpson*, 1980]. The main drawback with studying polymineralic rocks is that the kinematic framework at the grain scale can significantly deviate from simple shear due to strain partitioning between the different mineral/compositional domains [*Menegon et al.*, 2008]. In contrast, heterogeneous shear zones are rarely reported in monomineralic quartz mylonites [*Law et al.*, 1990]. Indeed only a few papers report an estimate of shear strain (γ) accumulated in analyzed quartz mylonite samples [e.g., *Lloyd et al.*, 1992]. Another limitation in applying data from experiments to field-based observations relates to the nature of the starting material. The grain size of the starting aggregates in experiments commonly differs from that of natural quartzites. Most experiments use fine-grained materials, whereas quartz mylonites were derived from coarse quartz crystals filling veins in some cases [e.g., *Pauli et al.*, 1996; *Stipp et al.*, 2002]. In addition, many experiments use starting material with no initial CPO, whereas natural quartz veins tend to have a strong starting CPO.

[5] Quartz cannot be deformed to large shear strain in the crystal-plastic regime with a Paterson gas-medium torsion apparatus, due to the limitation on the confining pressure that can be applied [*Kronenberg and Tullis*, 1984; *Tullis and Yund*, 1989; *Schmocker*, 2002]. However, large torsion experiments on many different geologically relevant, polycrystalline monomineralic aggregates (e.g., calcite: *Casey et al.* [1998], *Pieri et al.* [2001], *Barnhoorn et al.* [2004]; olivine: *Bystricky et al.* [2000]; anhydrite: *Heidelbach et al.* [2001]; halite: *Wenk et al.* [2009]) have all shown a strong dependence of the fabric with shear strain and a progressive change of type and strength of the CPO with increasing shear strain. These studies have also shown that a steady-state regime is only achieved, if ever, at very high strain (e.g., $\gamma = 11$ for calcite in the experiments of *Pieri et al.* [2001]) after a complex succession of transient mechanical, microstructural, and textural stages. A complex fabric evolution with increasing strain has also been recognized for naturally deformed calcite [*Oesterling et al.*, 2007] from an investigation of a heterogeneous shear zone within Carrara marble.

[6] Recent high-temperature experiments, using an all-NaCl assembly in a Griggs-type apparatus and a sample assembly as described by *Heilbronner and Tullis* [2002], have allowed noncoaxial deformation (with a dominant simple shear component) of fine-grained quartz aggregates in each of the three dislocation creep regimes [*Hirth and Tullis*, 1992] up to high shear strain ($\gamma = 8$) [*Heilbronner and Tullis*, 2006]. As with other minerals, these experiments shows a striking change in quartz CPO with increasing shear and degree of recrystallization over a large γ range. In detail, the CPO show: (i) a gradual change from a basal ⟨a⟩, to rhomb ⟨a⟩, and, finally, prism ⟨a⟩ dominated *c*-axis pole figures; (ii) a progressive rotation of the fabric skeleton with the sense of shear; and (iii) the development of a strongly domainal fabric in the high-strain, highly recrystallized samples. These recent results prompt several questions with regard to quartz. (i) Is the fabric evolution determined in experiments representative for natural quartzites especially those derived from coarse-grained veins? (ii) How much shear strain in nature is required to eventually achieve an invariant fabric? To answer these questions, there is the need to sample a series of quartz mylonites deformed over a large range of γ.

[7] In this paper, we document the microstructures and CPOs of sheared quartz veins from the Adamello tonalites. These veins were deformed by simple shear at temperatures above 500°C during the initial stages of postmagmatic

cooling of the pluton. The temperatures of emplacement and of plastic deformation of the veins were estimated by applying the Ti-in-quartz thermometer [*Wark and Watson*, 2006]. After this high-temperature deformation, the veins remained little deformed at lower temperatures. The veins have a tabular geometry and accommodated vein-parallel simple shear strain ranging from almost zero to >10. This case study represents an almost unique opportunity to analyze the CPO and microstructure evolution of quartz with increasing and measurable strain for a well-defined conditions and kinematic framework. This study emphasizes the role of initial growth CPOs in the veins in constraining their microstructural evolution and their strength (and thus amount of shear strain) during deformation at decreasing temperatures.

2. Geological Setting and Field Observations

[8] The studied quartz veins are hosted in the Avio tonalite (34–32 Ma old) of the Adamello batholith, southern Alps, Italy [*Pennacchioni et al.*, 2006]. The Avio pluton was emplaced at a depth of 9–11 km [*Pennacchioni et al.*, 2006], as constrained by the metamorphic assemblages in the northern and southern contact metamorphic aureole of the Adamello that yield P = 0.25–0.35 GPa [*Werling*, 1992; *John and Blundy*, 1993]. After emplacement, the tonalite cooled rapidly (over <4 Ma) [*Pennacchioni et al.*, 2006] to the ambient host rock temperatures of about 250°C. During this cooling, strike-slip ductile shear zones and later brittle faults developed. The shear zones and faults exploited two sets of pervasive, early postmagmatic, steeply dipping joints striking NNE and ESE in the study area (Lobbia outcrops, upper Genova Valley) and they show both sinistral (NNE–striking set) and dextral (ESE-striking set) sense of shear reflecting the NW–SE–directed regional shortening, which remained constant during the postmagmatic cooling of the pluton to the ambient conditions of intrusion [*Pennacchioni et al.*, 2006; *Mittempergher et al.*, 2009]. During the high-temperature stages, both joint sets were also locally filled with quartz veins that were subsequently subjected to plastic shearing [*Pennacchioni*, 2005]. The quartz veins studied in this paper all come from the dominant set of sinistral NNE-striking plastic shear zones. Left-lateral, NNE-striking ductile shear zones hosting quartz veins are spectacularly exposed on the flat, glaciated Lobbia outcrops. They are mostly strongly localized structures (derived from ductile shearing of quartz-filled joints) that are only a few millimeters thick, with sharp boundaries against the almost undeformed host tonalite. The quartz veins filling the joints are tabular in geometry for most of their length and range in thickness from a few millimeters to a few decimeters. The thickest veins are several meters long. Less commonly, quartz veins extended out of the joint plane, breaking through intact tonalite and forming extensional wings with a left-stepping orientation consistent with the left-lateral sense of movement on the shear zones. This observation suggests that vein opening was synkinematic with ductile shearing.

[9] The quartz veins are almost invariably weakly to strongly deformed and localize the ductile deformation, as commonly observed for quartz veins within granitoid rocks during amphibolite facies deformation [*Mancktelow and Pennacchioni*, 2005; *Pennacchioni and Mancktelow*, 2007]. They show an internal planar foliation oblique to the vein boundary and inclined antithetically (or counter-rotational) with the sense of shear (Figure 1). In most cases there is no or very little deformation of the host tonalite close to the vein boundary, but the sharp tonalite/quartz vein contact is commonly decorated by a dark millimeter-thick biotite-rich seam (Figure 1c). Where the host tonalite is deformed it has a sigmoidal foliation (Figure 1c), often forming paired mylonitic shear zones on both sides of the vein [*Mancktelow and Pennacchioni*, 2005; *Pennacchioni and Mancktelow*, 2007]. Tonalite mylonites, a few centimeters in thickness, are locally developed adjacent to the quartz veins (Figure 1d). The temperature of shear zone deformation is constrained to be ≥500°C by the synkinematic mineral assemblage (including stable $An_{38–40}$ plagioclase and biotite) of tonalite mylonites within the shear zones. The strong *c*-axis Y maximum of dynamically recrystallized quartz in an ultramylonitic quartzite [*Pennacchioni*, 2005] is consistent with this temperature estimate since this type of CPO was found to develop at $T \geq 500$°C in the mylonitic quartz veins within the metamorphic contact aureole of the northern Adamello by *Stipp et al.* [2002]. The shear strain γ_{fol} accommodated by the sheared quartz veins was estimated from the angle θ between the internal foliation and the vein boundary (Figure 1), according to the following equation [*Ramsay*, 1980]:

$$\tan 2\theta = -2/\gamma, \quad (1)$$

which is valid for simple shear deformation. A close approximation to simple shear is implied by the elongate tabular geometry of the quartz veins [*Ramsay*, 1980]. The estimate of γ_{fol} is affected by larger errors for small θ angles due to the dependence on tan2θ and the values calculated for highly sheared quartzites must be taken as only indicative. The total shear strain γ_{tot} across some quartz-bearing shear zones has also been estimated independently from the offset of aplite dykes, which are numerous in the Lobbia outcrops [see the map of Figure 3 of *Pennacchioni*, 2005], calculated as the ratio d/t (where d is the dyke offset and t is the quartz layer thickness). The estimated shear strains show that γ_{tot} is similar to γ_{fol} for low total strains (vindicating the use of equation (1) and the assumption of simple shear) but significantly larger in the case of high strains (e.g., at $\gamma_{fol} \sim 8$). The divergence between γ_{fol} and γ_{tot} is explained by localized boundary slip at the quartz-tonalite fine grained biotite-rich interface in the higher strain examples. Analysis of the distribution of the displacement along the shear zone based on marker offset [see Figure 6 of *Pennacchioni*, 2005] has revealed strong displacement gradients in most shear zones close to their tips. The differential displacement is accommodated by some deformation of the host tonalite, as indicated by the formation of foliated domains on the contractional sides of shear zone tips [*Pennacchioni*, 2005]. In such areas, the deformation deviates from simple shear and we specifically avoided sampling the shear zone tips.

[10] A series of 17 samples of weakly to strongly ($\gamma_{fol} \geq 15$) deformed quartz veins, all belonging to the NNE-striking set of ductile shear zone, were studied to investigate the evolution of microstructure and CPO with increasing strain.

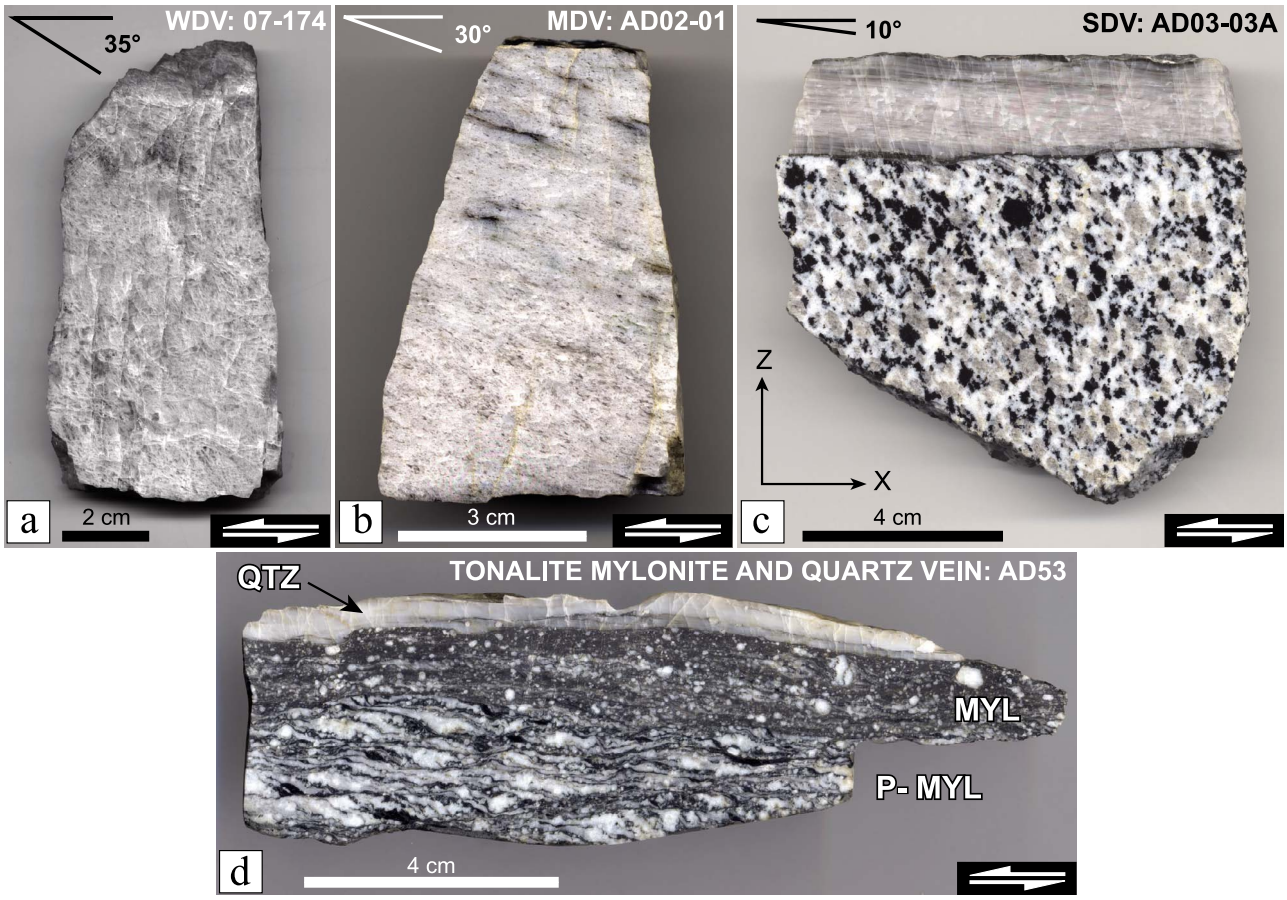

Figure 1. Polished samples of deformed quartz veins and of a tonalite mylonite. The quartz veins show an internal foliation oblique to the vein boundary and consistent with the sinistral sense of shear. (a) The weakly deformed vein (WDV) sample 07-174 shows a coarse grain size and an irregular foliation which is difficult to identify on the hand sample; the mean foliation orientation in the central left part of the sample is about 35° to the vein boundary (parallel to the base of the photo). (b) The moderately deformed quartz vein (MDV) sample AD02-01 shows a visible millimetric grain size. The foliation inside the vein is almost planar and inclined 30° to to the vein boundary (parallel to the base of the photo). The γ_{tot} and the γ_{fol} estimated for this sample are 1.2–2.2 and 2.3, respectively. (c) The strongly deformed quartz vein (SDV) sample AD03-03 shows a strong planar foliation oriented at a small angle (10°) to the vein boundary (corresponding to a $\gamma_{fol} \sim 10$). A thin dark biotite-rich seam is developed at the boundary with the host tonalite and there is an incipient development of a foliation in the tonalite close to the vein. (d) Tonalite protomylonite (P-MYL) and mylonite (MYL) flanking a sheared quartz vein (QTZ). The protomylonite includes discontinuous ribbons and elongated domains of deformed feldspar and quartz alternating with biotite-rich seams defining the foliation. The mylonite shows a dominant fine grained dark matrix with small rounded porphyroclasts of plagioclase. Sense of shear is sinistral as indicated by the shear bands in the protomylonite. All samples are cut perpendicular to the vein boundary (XY plane) and parallel to the lineation (X axis) (see the reference axes in (c)).

All samples come from a small area of a few thousands of square meters, where the ambient conditions of deformation are assumed to have been constant.

3. Microstructure

[11] The quartz microstructure was investigated by optical methods in thin (<30 μm) sections cut parallel to the lineation (X axis) and orthogonal to the foliation and to the vein boundary (XY plane). To measure the grain size and grain shape, grain boundary maps were made using the Lazy Grain Boundary macro and misorientation images, as described by *Heilbronner* [2000]. The samples have been categorized into three main types depending on the intensity of deformation, microstructure, and grain size (Figures 1 and 2): (a) weakly deformed veins (WDV; $\gamma_{fol} < 1$; samples: 07-139A-C, 07-140, 07-172, 07-174) (Figures 1a and 2a); (b) moderately deformed veins (MDV; $1 < \gamma_{fol} < 3$; samples: AD02-01, AD03-05, 07-142, 07-157, 07-163) (Figures 1b and 2b); and (c) strongly deformed veins (SDV; $4 < \gamma_{fol} < 15$; samples: AD03-03, AD03-06, AD03-07, AD03-09, GP06-01, 07-141) (Figures 1c and 2c). A tonalite mylonite

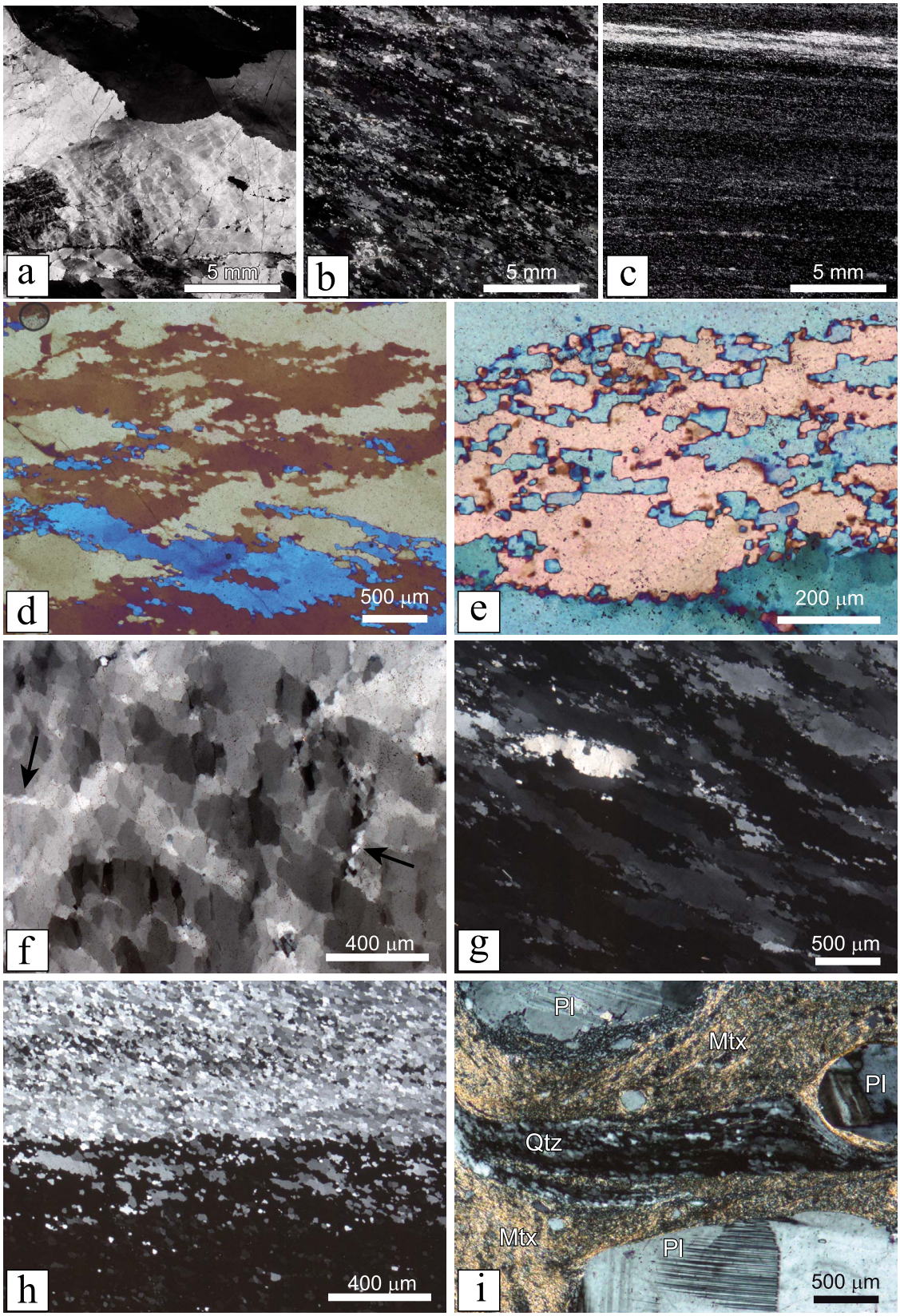
a
5 mm
b
5 mm
c
5 mm
d
500 μm
e
200 μm
f
400 μm
g
500 μm
h
400 μm
i
Pl
Mtx
Pl
Qtz
Mtx
Pl
500 μm

Figure 2

flanking a quartz vein was also investigated (sample AD53) (Figure 1d).

3.1. Weakly Deformed Veins

[12] The macroscopic samples do not show a well-formed strain-induced foliation. These samples consist of large (millimeter to centimeter in size) vein crystals (Figure 2a) preferentially elongated (and stretched) at an angle of 35°–45° to the vein boundary, with a consistent inclination relative to the sense of shear, corresponding to a shear strain $\gamma < 1$. The grain boundaries of these large crystals range from almost straight at the millimeter scale, except for a fine (micrometer scale) bulging, locally making a transition to thin aggregates of small new polygonal grains to extremely irregular jigsaw sutured shapes, including isolated islands of one grain within the adjacent one, indicative of tight 3D interfingering (Figures 2d and 2e). This interfingering microstructure of grains is more pervasive in the most deformed portions of the WDV and is interpreted to result from strain-induced fast grain boundary migration recrystallization. Under the microscope most grains show pervasive deformation microstructures, including heterogeneous, patchy extinction, and coarse polygonization to blocky subgrains (about 100 μm in size) (Figure 2f). The subgrains are arranged commonly in "chessboard"-type patterns of square to rectangular shape. The coarse polygonization is locally associated with smaller subgrains (<25 μm) and new grains developed along discrete, often discontinuous, seams (one to a few new grains thick) that form subparallel sets or conjugate arrays (Figure 2f). The measured grain size of the new fine recrystallized grains in sample 06-139D is 34 ± 17 μm. In detail, the deformation is markedly heterogeneous.

[13] The quartz crystals locally include microboudinaged clasts of the host rock plagioclase that are stretched in the same direction as the host grain elongation and with open space between individual fragments filled with quartz in crystallographic continuity with the host grain. This indicates progressive crack sealing during vein quartz growth, as do some thin seams of biotite inside the vein that outline discrete surfaces subparallel to the vein boundary.

[14] Small (mainly a few microns in size) fluid inclusions are common to locally abundant. They occur commonly as subparallel trails controlled by the crystallography of the host grain or decorate the coarse subgrain boundaries in deformed regions of quartz crystals. Other fluid inclusion trails crosscut the grain boundaries without deflection.

3.2. Moderately Deformed Veins

[15] These veins show a well-developed foliation and a coarse grain size visible in hand specimen. The foliation is defined by the preferred elongation of grains and ribbons (Figures 2b and 2g), and the estimated γ_{fol} is in the range of 2 to 3. The shape of grains is highly serrated to skeletal in some cases (e.g., sample 07-157). As in the case of WDV, microscopic investigation reveals that, in many cases, some separate grains have the same crystallographic orientation and actually belong to a common parent grain. This implies a complex interfingering grain structure in 3D. Some of these parent grains are stretched to form ribbons extending for the whole length of the thin section, especially in the case of crystals with a *c*-axis orientation close to the Y direction, which are dominant in these rocks, as indicated by the dark to black color of most grains under crossed polars. A few grains have relatively low aspect ratio and behave as porphyroclasts that are wrapped around by the elongate grains and ribbons. These grains often show marginal recrystallization to fine (average grain size of 35–38 μm) aggregates and have a bright white color under crossed polars (Figure 2g). The new recrystallized fine grains in MDV form only a small (<5%) volume. The grains of MDV are polygonized but the subgrain size is smaller (<50 μm) than in WDV. The serrated outline of the grains is determined in part, on a fine scale, by a rim of equant polygonal small new grains forming aggregates either one grain or several grains wide. Compared to serrated grains in WDV the elongation and degree of serration/intefingering appear to be more strongly developed and pervasive.

3.3. Strongly Deformed Veins

[16] These veins consist of almost completely recrystallized aggregates of new grains of grain size in the range of 34–40 μm, and there is no systematic variation of grain size with increasing shear strain above $\gamma \sim 4$. The estimated γ_{fol} of these samples is larger than 4 and up to over 15. Thus recrystallization occurs rather abruptly in a narrow range

Figure 2. Optical microstructures of deformed quartz veins. (a–c) Comparative microphotos of the microstructures of WDV (sample 07-140), MDV (sample AD02-01), and SDV (sample AD03-09), taken under crossed polars and same magnification. The vein boundary is parallel to the base of the photos. (d–i) Details of the microstructures. (d) Irregular, strongly serrated grain boundaries with islands of one grain enveloped by adjacent ones, and crossed polars and gypsum plate; sample 07-139D (WDV). (e) Interpenetrated grains with an archipelago of island grains (blue) belonging to a single parent crystals interlocking with a neighboring grain (yellow). Individual islands show rational right-angle boundaries with the host grain. Crossed polars and gypsum plate; sample 07-139D (WDV). (f) Coarse blocky subgrains within a large single crystal. Arrows indicate incipient thin seams of overprinting, smaller subgrains and new grains along conjugate sets of planes. Crossed polars; sample 07-140 (WDV). (g) Elongate ribbon grains defining the foliation in a MDV. These dominant grains have dark extinction colors in contrast to the relatively low aspect ratio, bright grain in the upper left quadrant of the photo. Note that fine recrystallized grains are almost absent. Crossed polars: sample 07-142 (MDV). (h) Extinction banding in a finely recrystallized mylonitic quartz vein. The small grains are slightly inclined oblique to the banding/foliation, consistent with the sinistral sense of shear. The foliation (horizontal in the photo) is inclined of an angle of ca. 10° to the vein boundary. Crossed polars; sample AD03-06 (SDV). (i) Ribbon of recrystallized quartz (Qtz) and large plagioclase porphyroclasts (Pl) within the biotite-rich (biotite ± quartz ± plagioclase ± ilmenite) matrix (Mtx) of a tonalite mylonite. Crossed polars; sample AD53.

of shear strains between 3 and 4. The fine recrystallization occurred by dominant subgrain rotation recrystallization. Under the microscope and with crossed polars, the foliation is typically defined by extinction domains of recrystallized grains (Figure 2h), but with a clear predominance, in most of the samples, of dark domains with the quartz *c* axes oriented close to the Y axis. The orientation of the extinction domains coincides with the orientation of the foliation visible in polished samples. The new recrystallized grains are either equant or, more commonly, elongate with their long axes defining a shape preferred orientation (SPO) oblique to the foliation and to the vein boundary (Figure 2h). The angle δ between the SPO and the vein boundary was measured by image analysis from automatically digitized grain boundaries. Only grains with aspect ratio >2 were considered in order to avoid artifacts due to digitization. The maxima (more than 30% of grains) of the angle δ between the grain long axis and the vein boundary in the different samples ranges between 42° and 58° with an average value in SDV of 51.5°.

3.4. Tonalite Mylonites

[17] Tonalite mylonites consist of a fine-grained matrix of quartz, plagioclase (andesine in composition), biotite, and ilmenite, including rounded porphyroclasts of plagioclase and elongated ribbons of quartz (Figure 2i). These quartz ribbons derived from deformation and complete recrystallization to fine aggregates of the magmatic quartz. The recrystallized grain size is variable, due to strong strain gradients associated with the presence of the large plagioclase porphyroclasts wrapped around by the quartz ribbons and is on the order of a few tens of micrometers (with the finest grain size <10 μm). The quartz aggregates have commonly SPO (consistently inclined with the sense of shear) and have a dark color under crossed polars, indicative of a CPO with a strong Y maximum of the *c* axes. Alteration of biotite to chlorite and of oligoclase to albite is absent to very minor and postkinematic. This suggests that the mylonites were preferentially developed under high temperature (corresponding to conditions of the amphibolite facies in metamorphic rocks) and were not later overprinted during lower temperature stages of pluton cooling.

4. Crystallographic Preferred Orientation

4.1. Methods

[18] The CPO of quartz was determined by X-ray texture goniometry (TG) and, for the *c* axes alone, by computer-integrated polarization microscopy (CIP) [*Panozzo Heilbronner and Pauli*, 1993; *Heilbronner*, 2000]. Details on these techniques can be found in the Appendix A. While X-ray diffraction allows a volume-related, quantitative texture analysis, the CIP-method gives instead a grain- or microstructural domain-related determination of the *c*-axis directions, which can be visualized by an "Achsenverteilungsanalyse" (AVA, axis distribution analysis) [e.g., *Sander*, 1950; *Trommsdorf and Wenk*, 1963]. The thin sections used for the CIP analysis (and for the microstructural analysis) were prepared from mirror sample chips of those used for the X-ray analysis.

4.2. The CPO in WDV

[19] All the WDV samples, except 07-172, show a dominant single-crystal type orientation with the *c* axes oriented in the XZ plane and rotated by a small anticlockwise (synthetic) angle to the foliation (and therefore at a high angle to the crystal elongation), with distinct ⟨a⟩ axis maxima (Figure 3). This is by far the volumetrically dominant CPO in samples 07-139A-C and 07-174, though crystals with different crystallographic orientations are visible in thin sections. Samples 07-139D and 07-140 show additional *c*-axis maxima mostly distributed along the diameter of the pole figure connecting the peripheral maxima: (i) in the *Y* direction and (ii) in the intermediate position between the periphery and the Y maximum. Together the *c*-axis maxima define a kind of a girdle oriented at a low synthetic angle to the vein boundary. Sample 07-139D also shows two *c*-axis maxima at high angle to the vein boundary and a weak peripheral maximum of this type is also visible in the pole figure of sample 07-174. Sample 07-172 has a CPO that differs somewhat from the rest of the WDV. The *c*-axis maxima are oriented at a low to intermediate angles to the vein boundary and seem to form two main girdles distributed symmetrically to the foliation. The strongest *c*-axis maxima are still at the periphery but in a mirror-symmetric position (i.e., rotated in an antithetic sense) to the maxima of the other WDV through the YZ plane. In summary, the WDV do not have a random crystallographic orientation, but the CPO shows a dominant crystal *c*-axis direction oriented at a low angle to the vein boundary and therefore at a high angle to the deformation-induced CPO developed in the MDV and SDV as described below.

4.3. The CPO in MDV

[20] The texture goniometer analysis indicates that a strong bulk CPO of the *c* axes, defining a partial YZ girdle concentrated near Y, was already achieved in some MDV (samples AD03-05 and AD02-01) (Figure 4) for a shear strain in the range of 2 to 3. This type of CPO is also characteristic of the SDV, as will be described in the next section. The *c*-axis partial YZ girdle shows a very slight sigmoidal shape with the tips of the girdle synthetically inclined with the sense of shear from the Z direction. The ⟨a⟩ pole figures have six distinct maxima (though with some streaking-out in the concentration at the periphery of the pole figure) with the strongest one oriented at a small synthetic angle to the lineation. The CPO is consistent with dominantly prism ⟨a⟩ and subordinate rhomb ⟨a⟩ slip. The individual pole figures of AD03-05 and, as reported in Figure 5, of AD02-01 measured from different sample areas (3 and 6 areas, respectively, each of a size of ca. 1 cm^2) are almost identical to the bulk CPO reported in Figure 4. This means that the CPO of these two samples is almost homogeneous at the scale of about 1 cm^2. The pole figures of the other MDV samples show, in addition to the elongate Y maximum described above, features somewhat reminiscent of the CPO of WDV. Indeed a weak *c*-axis maximum orthogonal to Y and near the lineation can be observed in the texture goniometer pole figure (site 2) of Figure 5. This is clear in the *c*-axis pole figure of the sample 07-157 (Figure 4), which can be interpreted as a combination between (i) a new partial YZ girdle and (ii) a girdle

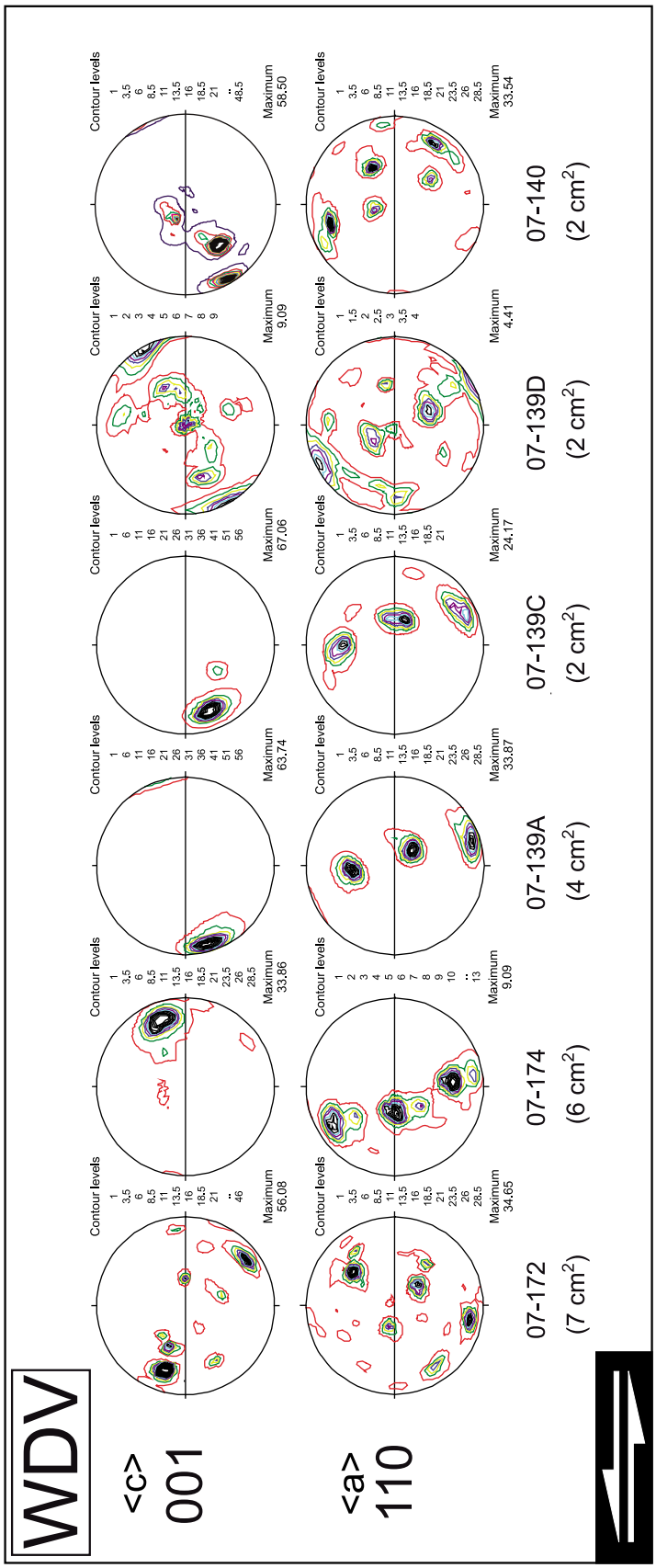

Figure 3. Plots (equal area, upper hemisphere projections) of ⟨c⟩ and ⟨a⟩ axes of the WDV determined by texture goniometry. The plots (equal area, lower hemisphere) are cumulative and the total area investigated in each sample is reported below the sample label.

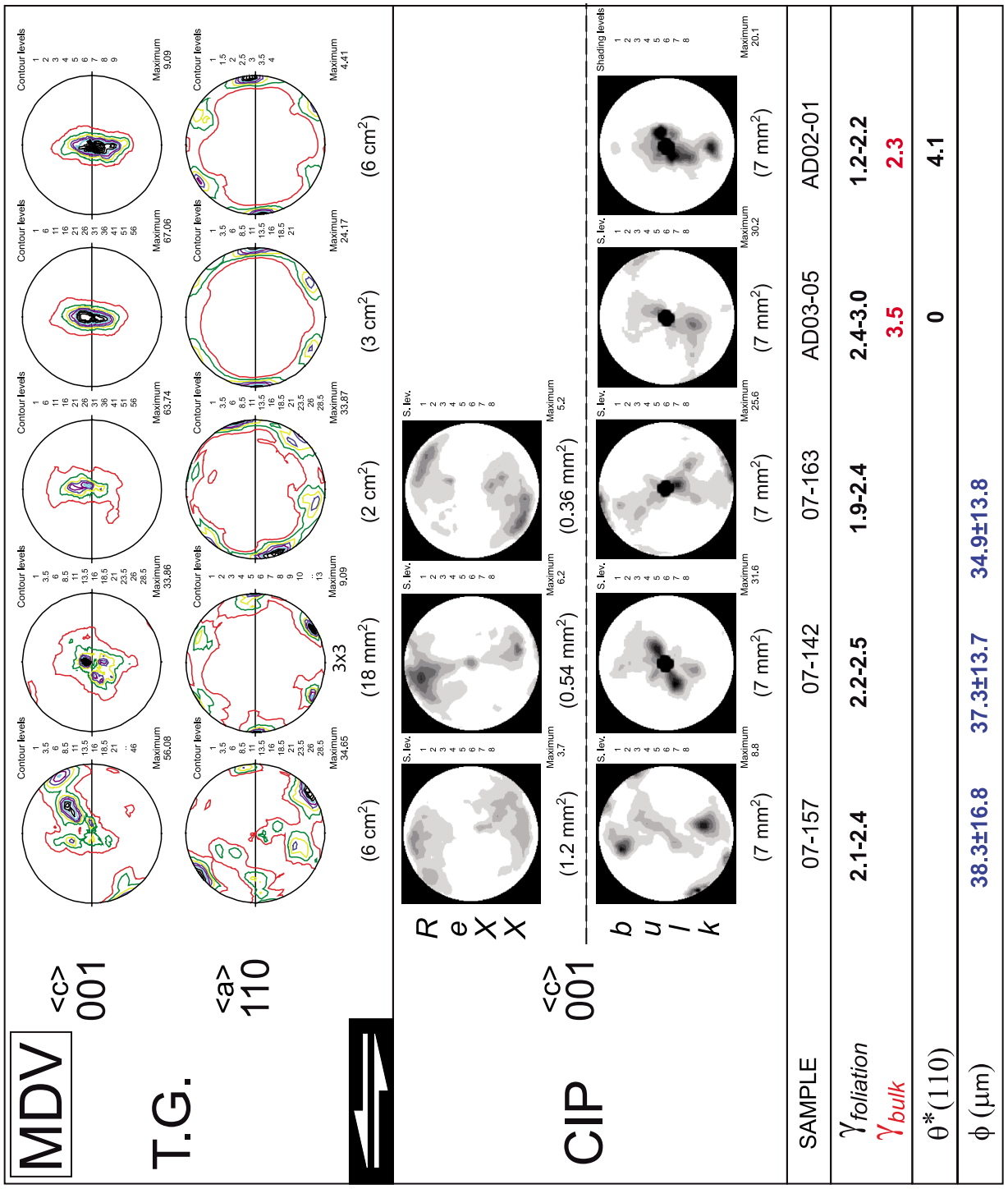
MDV
T.G.
<c> 001
<a> 110
(6 cm²)
(18 mm²)
3x3
(2 cm²)
(3 cm²)
(6 cm²)
Contour levels
Maximum
Shading levels
S. lev.
R e X X
CIP
<c> 001
b u l k
(1.2 mm²)
(0.54 mm²)
(0.36 mm²)
(7 mm²)
SAMPLE
07-157
07-142
07-163
AD03-05
AD02-01
γ foliation
γ bulk
2.1-2.4
2.2-2.5
1.9-2.4
2.4-3.0
3.5
1.2-2.2
2.3
θ*(110)
0
4.1
ϕ (μm)
38.3±16.8
37.3±13.7
34.9±13.8

Figure 4

orthogonal to XY and slightly rotated in a synthetic sense with the sense of shear with respect to the foliation. This pattern is very similar to that measured in the WDV sample 07-139D. The *c*-axis distributions of samples 07-142 and 07-163 can be approximated as a partial YZ girdle concentrated near Y, but they have a more irregular shape than those for samples AD03-05 and AD02-01, perhaps due to some remnant features of the early fabric. The CPO of sample 07-142 also shows a very weak peripheral maximum at a high angle to the foliation suitably oriented for basal ⟨a⟩ slip.

[21] CIP analysis reveals local textural heterogeneity at a scale smaller than 1 cm^2 (i.e., the spot size investigated by texture goniometer) even in the case of samples with a well-developed CPO. Figure 6 shows the different *c*-axis pole figures determined by CIP analysis for sample AD03-05. Though most CIP pole figures approximate a partial YZ girdle similar to the bulk CPO, in two cases (pole figures 7 and 8) the CPO records a relict girdle inclined at a synthetic angle to the foliation, which is typical of most WDV. This relict textural component was not detected in the CPO determined by texture goniometer on larger investigated areas.

[22] CIP analysis is useful to investigate the relationships between microstructure and texture. In samples 07-163 and 07-157 the analyses focused on sites containing relatively low-aspect-ratio grains. Grains from these sites show strong internal distortion and polygonization but behaved as relatively hard domains in the quartz aggregate, deflecting the surrounding elongated quartz domains. These quartz porphyroclasts have their *c* axes oriented at a high angle to the foliation (Figures 7a and 7b). CIP analysis was also used to determine the CPO of the fine-grained recrystallized aggregates in MDV (Figure 4). In the three investigated cases, these aggregates all show a CPO with *c*-axis scattering mainly at a high angle to the vein boundary, though with a tendency to form a girdle, with an asymmetry both in a synthetic (samples 07-157 and 07-142) and antithetic (sample 07-163) sense relative to the sense of shear.

4.4. The CPO in SDV

[23] With the exception of sample AD03-06, the SDV show a strong bulk CPO characterized by *c* axes distributed in a partial YZ girdle concentrated near Y (Figure 8). The *c*-axis CPO has an almost orthorhombic symmetry or is slightly asymmetric, with the tips of the *c*-axis girdle slightly bent in the direction of shear. The CPO asymmetry is more accentuated in the CIP pole figures. Sample AD03-06, which records a small estimated shear strain of the SDV suite, differs by showing an almost complete single girdle in the bulk pole figure, inclined with the sense of shear at a high angle to the shear plane and a much weaker maximum at Y. Compared with the CPO of samples AD03-05 and AD02-01 (MDV), the *c*-axis partial girdles of samples GP06-01 and 07-141 (SDV) are shorter and have almost shrunk to a single Y maximum. However, they are almost identical to the CPOs of samples AD03-03A, AD03-07, and AD03-09, despite the large difference in shear strain.

[24] The ⟨a⟩ axes show strong and well-defined maxima at the periphery of the pole figure, with two main maxima forming a small angle antithetic to the lineation. Some tendency for a distribution of the ⟨a⟩ axes in a rotational sense around the central *c*-axis maximum can be seen in the CPO. The angle θ^*, that is, the angle formed by the ⟨a⟩ maximum with the lineation, ranges from 2.3° to 16° without a systematic variation with shear strain. In general, the CPO of the SDV is therefore rather strain insensitive at the scale of 1 cm^2 and can be considered to be in a steady state. This is associated with an invariant grain size and average orientation of the SPO, which also suggests the achievement of a steady-state texture and microstructure for shear strain above ca. 4.

[25] The bulk CPO does not fully reflect the local textural complexity of these quartz mylonites, which all include a domainal CPO with alternating bands (several tens of microns to a millimeter in thickness) showing different extinction patterns. The CIP analysis in part focused on discriminating the different CPO in these adjacent domains: this explains why the cumulative pole figure obtained by CIP differs somewhat from the bulk CPO. An example of such banding is shown in Figure 9 for sample AD03-03A. Figure 9a shows the optical microscope image of the thin section under crossed polars with the area investigated by CIP outlined (enlarged in Figure 9b), showing extinction domains delineating the foliation. The bulk CPO in Figure 9c (for an area of about 1 cm^2) is dominated by *c* axes close to the Y direction, typical of the SDV. However, the CPO of individual domains can differ substantially and, in the case of the selected site of Figure 9b, shows a single girdle pattern (Figure 9d), although still with a strong Y maximum. To highlight *c*-axis orientations corresponding to the activity of the main slip systems in quartz (i.e., basal ⟨a⟩, rhomb ⟨a⟩, and prism ⟨a⟩ slip) a particular look-up table (LUT), shown below the *c*-axis orientation images (COI) of Figure 9e, has been applied following the method suggested by *Heilbronner and Tullis* [2006]. The calculated COI (Figure 9e) suggests that all three main slip systems operated locally. The contribution of the individual slip system is evident in the exploded bitmaps of Figures 9f–9h. As can be estimated qualitatively in Figure 9, there is a large dominance in the dark domains over the gray and bright bands, which explains the bulk pole figure dominated by a *c*-axis orientation near *Y*.

[26] The bulk *c*-axis pole figure of sample AD03-06, showing an almost complete single girdle as in the case of the local CIP pole figure of Figure 9d, results from the presence of large (several millimeters thick and extending

Figure 4. CPO (⟨c⟩ and ⟨a⟩ axes) measured by both texture goniometry (TG) and CIP of the MDV. All the pole figures (equal area, upper hemisphere projections) are cumulative ones and derived from different measurements in the samples. The CIP plots refer to both the fraction of recrystallized grains (ReXX row) and to the overall *c*-axis orientation of the investigated area (bulk row). The total investigated area is reported below the pole figures. The figure also reports for each sample: the estimated shear strain of the sample (γ_{fol} and, where determined, the γ_{bulk}, as defined in the main text), the angle θ^* (formed by the ⟨a⟩ maximum and the foliation), and the grains size ϕ of recrystallized grains.

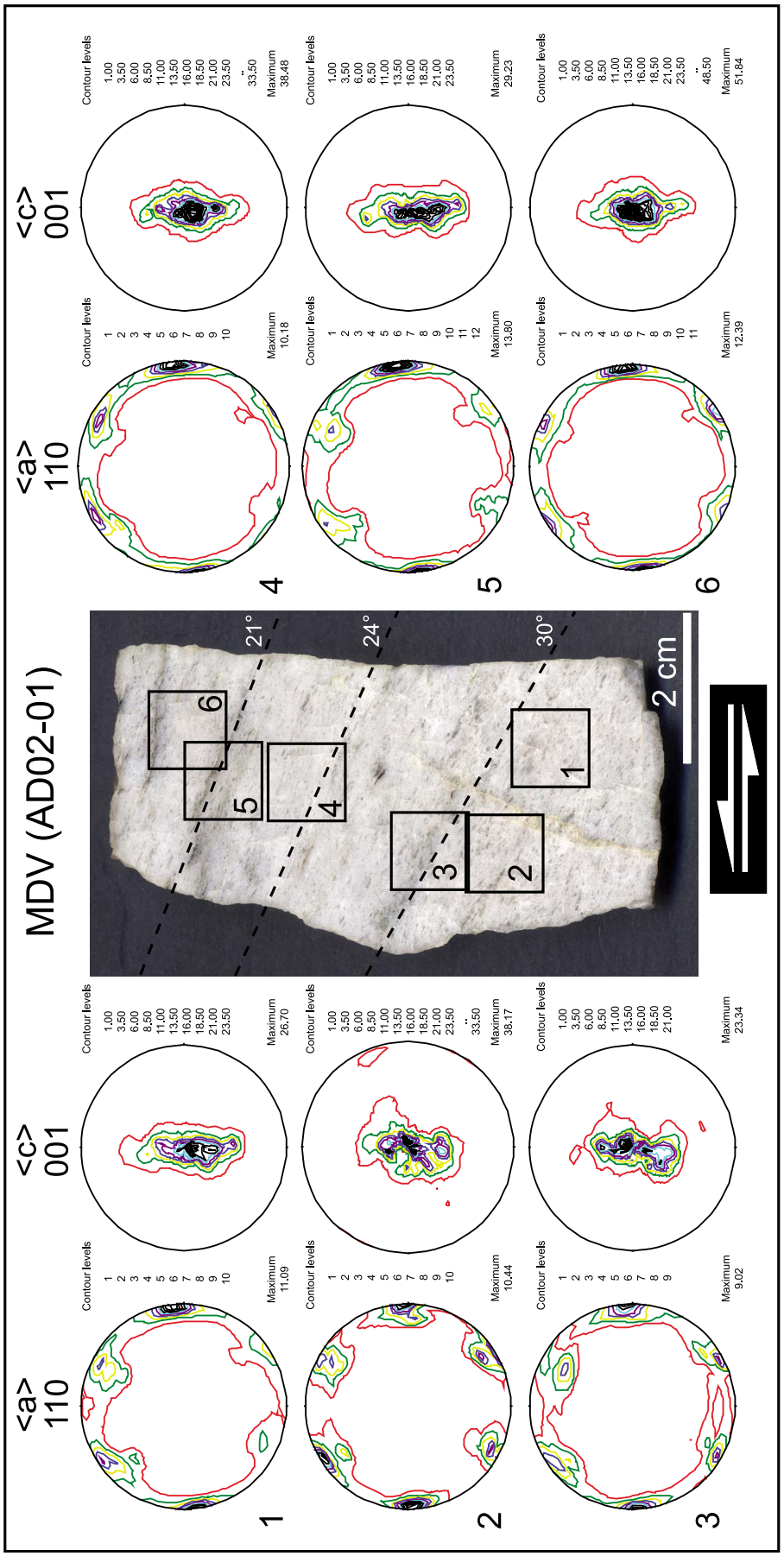

Figure 5. Individual texture goniometer pole figures (equal area, upper hemisphere projections) taken at six different areas (indicated on the photo of the polished sample) of the MDV sample AD02-01. The dashed lines drawn on the samples outline the foliation (the angle of inclination to the vein boundary is reported to the right). The γ_{fol} for the sample ranges from 1.2 to 1.8–2.2 in the lower (spots 1–3) and upper (spots 4–6) part of the sample. All the individual pole figures are very similar or identical to the bulk pole figure reported in Figure 4, and the CPO is, therefore, homogeneous on the scale of about 1 cm^2. However, note that site 2, from the less deformed part of the sample, shows a weak component of the CPO referable to a girdle slightly inclined to the foliation, recalling the CPO of the WDV.

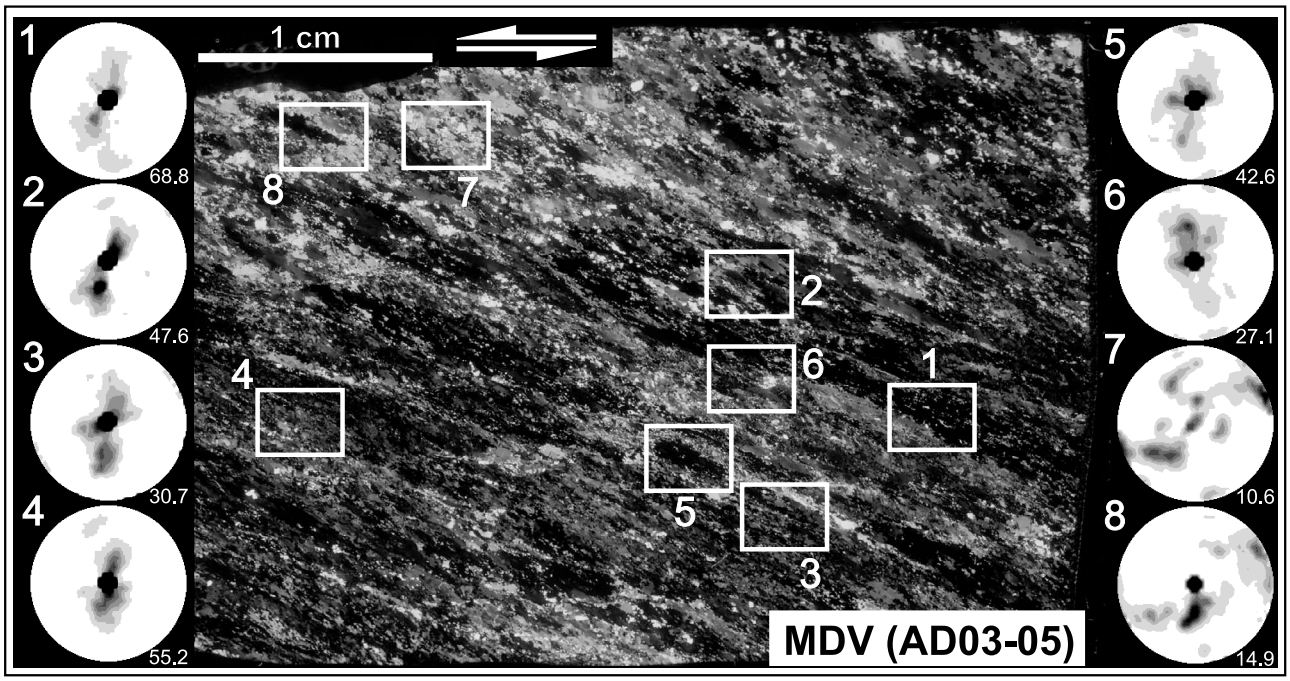

Figure 6. Small-scale (<1 cm^2) heterogeneities of the *c*-axis CPO revealed by the CIP analysis (MDV sample AD03-05). Though most of the pole figures (sites 1–5) can be approximated by a short single girdle with a strong Y maximum of the bulk CPO (site 4), some of the CIP pole figures show other fabric components including basal ⟨a⟩ maxima (4–8) and maxima forming a low angle girdle to the foliation (7–8), as in the WDV. The presence of fabric heterogeneity, clearly seen from simple visual investigation of the optical microphoto (entire thin section, crossed polars), disappears in the bulk texture goniometer pole figure of Figure 4.

across the whole thin section length) recrystallized bands with light extinction tones, indicative of dominant rhomb ⟨a⟩ and basal ⟨a⟩ slip (Figure 10). The size of these bands is consistent with the coarse grain size of quartz crystals in the starting material and the CPO domains can be interpreted as inherited from original growth sizes and orientation of quartz crystals.

5. Ti Concentrations in Quartz

[27] The Ti concentration in quartz was determined by SIMS (Cameca IMS 4f) at the Edinburgh Ion Microprobe Facility (EIMF), University of Edinburgh, in four samples (1 WDV: AD07-174; 3 SDV: AD03-03A, AD03-07, and AD53), with the aim of applying the Ti-in-quartz thermometer calibrated by *Wark and Watson* [2006]. Details on the measurement technique can be found in Appendix B. The measured Ti contents of quartz are reported in Table 1. In the SDV the Ti content is rather homogeneous throughout each sample and remarkably similar among the different samples, ranging between 4.6 and 5.7 ppm. In terms of temperature this equates to a maximum variation of about 25°C between the samples. In sample AD53, the two investigated quartz sites in the tonalite mylonite yield Ti contents either comparable to those of the SDV (4.3 ppm) or higher (13.6 ppm), which reflects the origin of these recrystallized grains from magmatic quartz and their subsequent reequilibration to the synkinematic temperatures. The Ti content in the WDV 07-147 is slightly variable and higher than in SDV but basically similar in terms of inferred temperatures.

6. Discussion

6.1. The Natural Lab of Quartz Deformation in the Lobbia Outcrops

[28] Several observations imply that quartz veins of the Lobbia outcrops are especially suitable and provide an almost unique case for studying the evolution of the microstructure and CPO of quartz with increasing strain.

[29] 1. The structural and thermal evolution of the Adamello tonalite is simple. The solid-state deformation history of the tonalite and of the quartz veins developed during rapid cooling of the pluton to the host rock ambient conditions at the base of the brittle crust (≤250°C). These rocks were not involved in any successive thermal event. Therefore postkinematic effects and annealing processes are negligible.

[30] 2. Thermal conditions during veining and shearing were almost constant as indicated by the mineral assemblage of the mylonites associated with the sheared quartz veins and by Ti-in-quartz data.

[31] 3. Numerous quartz-bearing shear zones can be sampled in a restricted area.

[32] 4. The veins filled precursory planar joints and have a tabular geometry for most of their length. They localize the

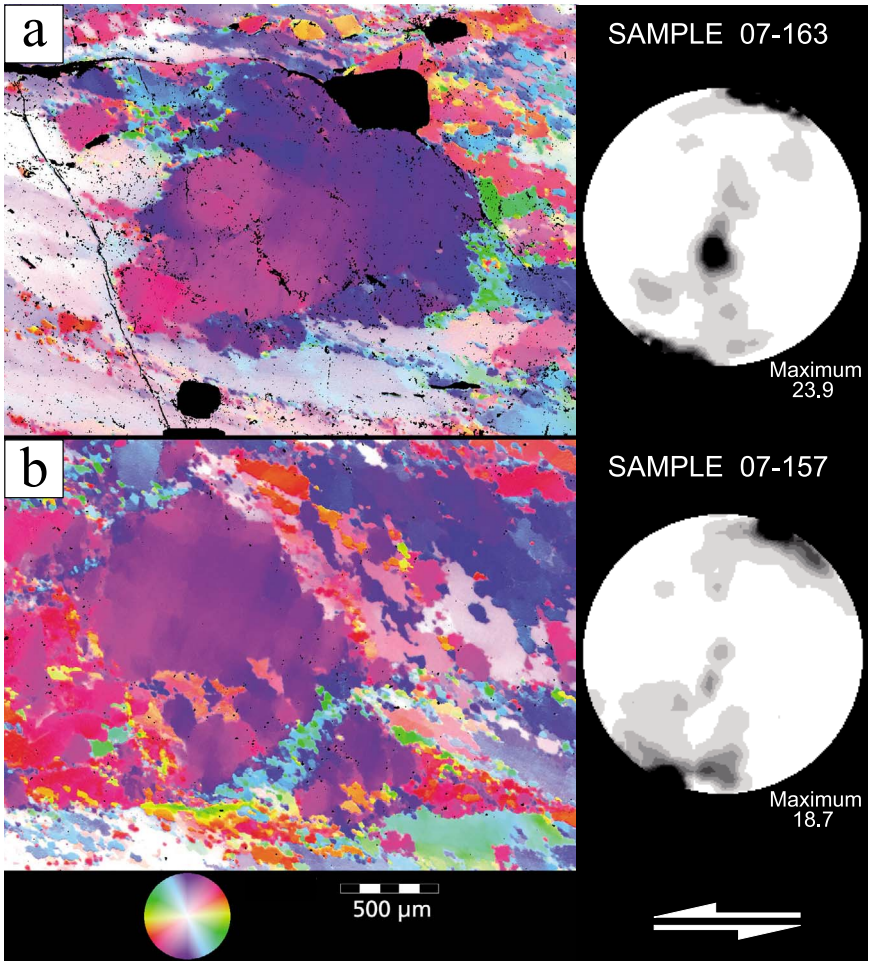

Figure 7. COIs (*c*-axis orientation images) and CIP pole figures (equal area, upper hemisphere projections) of low-aspect-ratio "porphyroclasts" in the MDV (samples 07-157 and 07-163). Both porphyroclasts have a *c* axis at a low angle to the foliation in an orientation suitable for basal ⟨a⟩ slip (the strong *c*-axis Y maximum of pole figure of sample 07-163 is related to the elongate grains surrounding the porphyroclast).

deformation within the almost undeformed tonalite, constraining the strain geometry to be effectively simple shear parallel to the vein boundary.

[33] 5. The outcrop contains numerous aplite dykes that are crosscut by the quartz veins and shear zones. This allows the total strain accommodated along the sheared zone quartz veins to be estimated in many cases. Up to moderate deformation, the shear strain estimate based on the inclination of foliation within the veins (using equation (1)) and on the aplite offset correspond, confirming that deformation was effectively simple shear.

[34] 6. The numerous quartz veins record a broad spread in shear strains, with the investigated samples covering a range of γ from less than 1 to >15.

[35] 7. All MDV and SDV show an almost planar strain-induced foliation indicative of a rather homogeneous deformation.

6.2. Temperature of Quartz Veining and Ductile Deformation

[36] According to *Stipp et al.* [2002] the transition from combined basal, rhomb, and prism ⟨a⟩ slip to dominantly prism ⟨a⟩ slip (and therefore from a YZ girdle to a dominant single Y maximum in the *c*-axis pole figures) is rather abrupt and occurs at about 500°C. Given the Y maximum CPO of most of the SDV, 500°C can be assumed as a minimum temperature for deformation of the quartz veins. Such a temperature can be independently

Figure 8. CPO (⟨a⟩ and ⟨c⟩ axes) measured by both texture goniometry and CIP of the SDV. All the pole figures (equal area, upper hemisphere projections) are cumulative ones and derived from different measurements in the samples. The total investigated area is reported below the pole figures. The figure also reports for each sample: the estimated shear strain of the sample (γ_{fol} and, where determined, the γ_{bulk}), the angle θ* (formed by the ⟨a⟩ maximum and the foliation) and the grains size ϕ of recrystallized grains.

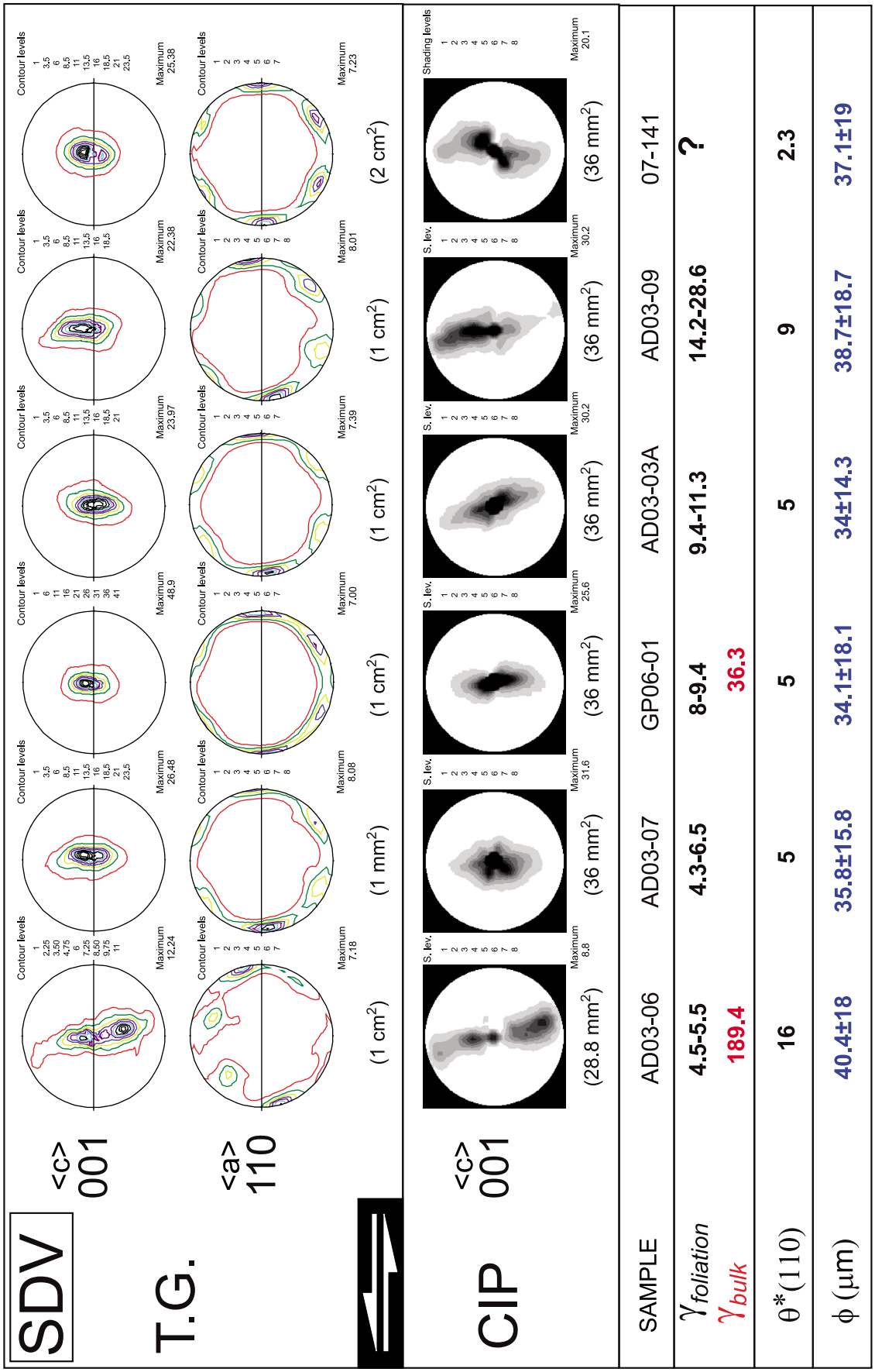

SAMPLE	AD03-06	AD03-07	GP06-01	AD03-03A	AD03-09	07-141
$\gamma_{foliation}$	4.5-5.5	4.3-6.5	8-9.4	9.4-11.3	14.2-28.6	?
γ_{bulk}	189.4		36.3			
$\theta^*(110)$	16	5	5	5	9	2.3
ϕ (μm)	40.4±18	35.8±15.8	34.1±18.1	34±14.3	38.7±18.7	37.1±19

Figure 8

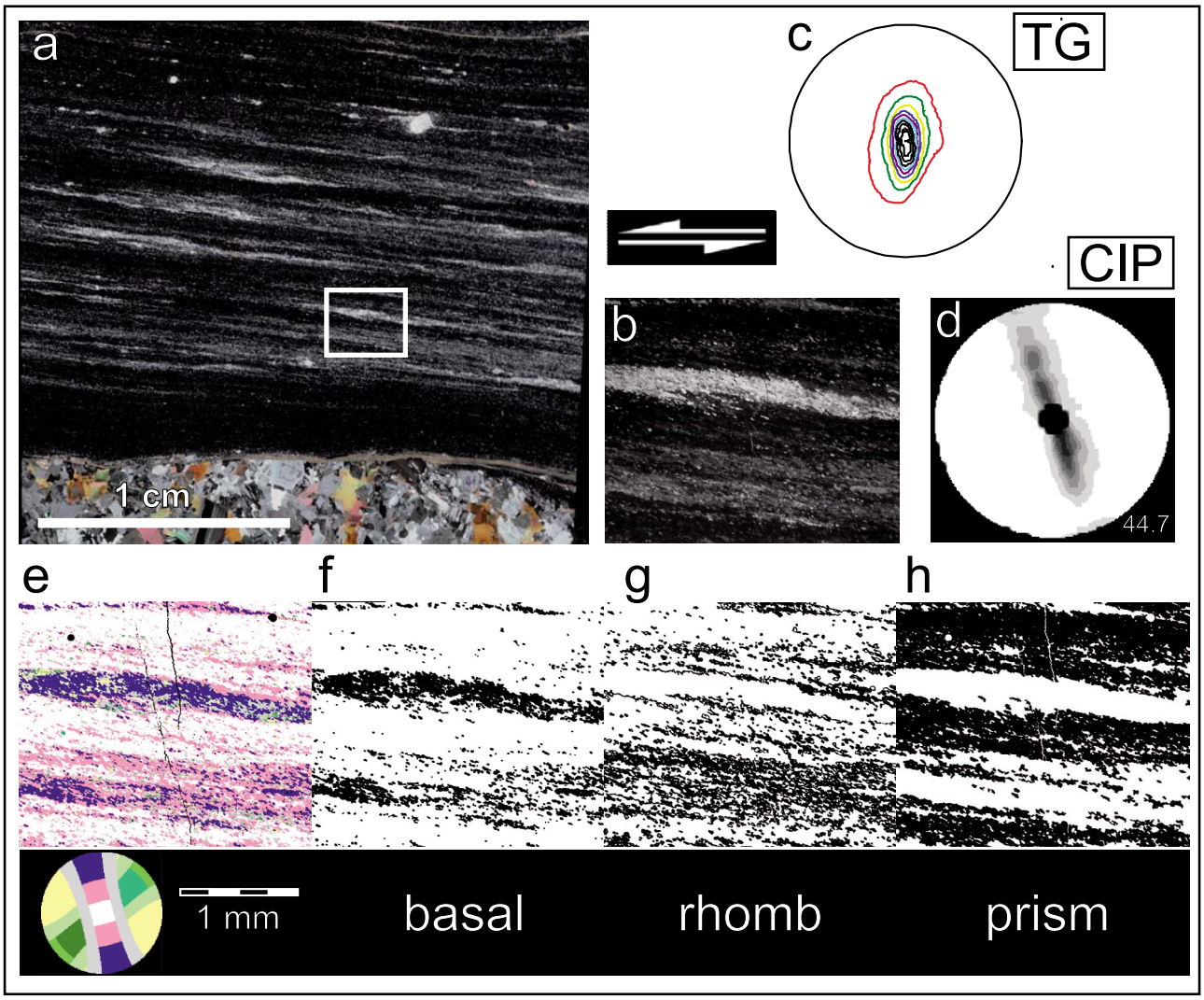

Figure 9. Local scale fabric heterogeneity in SDV (sample AD03-03A). Optical microphotograph (a) of the thin section under crossed polars with area outlined that was investigated by CIP (enlarged in Figure 9b), where the extinction banding delineating the foliation is clearly visible. The bulk CPO in Figure 9c (relative to an area of about 1 cm^2) is dominated by *c* axes close to the *Y* direction, typical of the SDV. Figure 9d is the CPO measured by CIP for the area in Figure 9b. Figure 9e shows the *c*-axis orientation image of the area analyzed by CIP colored using the look-up table (LUT) shown on the bottom side. Three extracted bitmaps show domains in black suitably oriented for basal ⟨a⟩ (Figure 9f), rhomb ⟨a⟩ (Figure 9g), and prism ⟨a⟩ glide (Figure 9h).

inferred for the main deformation phase in the Lobbia based on the mineral assemblage of the associated tonalite mylonites [*Pennacchioni et al.*, 2006].

[37] A precise estimate of the deformation temperature in the quartz veins is potentially possible by applying the Ti-in-quartz thermometer proposed by *Wark and Watson* [2006] (see Appendix C). The temperature of a rutile-undersaturated assemblage can be calculated, provided the TiO_2 activity is known, by the following equation:

$$T(^{\circ}\mathrm{C}) = \frac{-3765}{\log\left[\frac{X_{\mathrm{Ti}}^{\mathrm{qtz}}}{a_{\mathrm{TiO_2}}}\right] - 5.69} - 273. \qquad (2)$$

The temperatures calculated for $a_{TiO_2} = 1$ with equation (2) in the Adamello samples are reported in Table 1 and range between 470° and 500°C for SDV and about 505°C for the WDV sample. These temperatures should be considered minimum temperatures (assuming Ti equilibration in the vein) because the Adamello quartz veins contain neither rutile nor any other Ti mineral (therefore $a_{TiO_2} < 1$). An estimate of the TiO_2 activity in the monomineralic quartz veins is not possible and this can result in a large underestimate of the actual deformation temperature. Given the measured Ti contents, for $a_{TiO_2} = 0.4$ the calculated temperatures are 65°–75°C higher than for rutile-present conditions (Table 1). However, in the tonalite mylonite of sample AD53 ilmenite is a major component in the mylo-

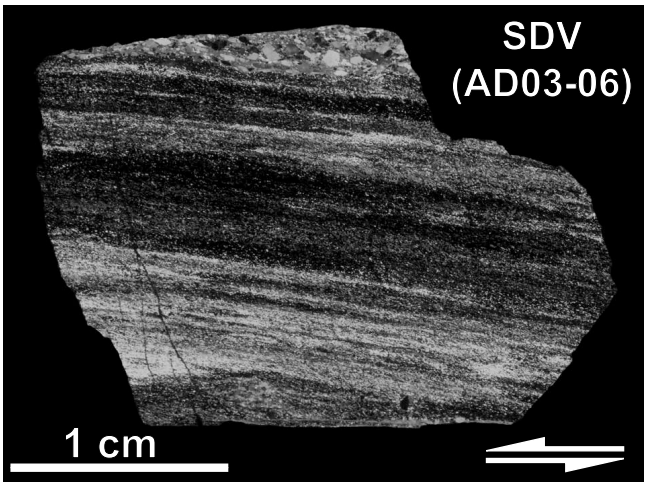

Figure 10. Optical microphotograph (crossed polars) of the SDV sample AD03-06 (γ = 4.5–5.5). The upper right corner of the sample is a sheared tonalite. Within the vein, the foliation is defined by a CPO banding, as seen from large gray to white extinction domains alternating with dark domains. This CPO banding is believed to derive from coarse original vein crystals with different orientations. The domain investigated by texture goniometry is an area of about 1 cm^2 centered in the middle of the sample.

nitic matrix, and the magmatic quartz (with presumably an initial Ti content on the order of 250 ppm) has recrystallized to fine-grained aggregates. In this case a_{TiO_2} = 0.4 can be assumed as a minimum value [*Wark and Watson*, 2006] and the corresponding maximum temperature of deformation is 540°C.

[38] Independently of a precise estimate of the deformation temperature (which is beyond the scope of the current paper), the Ti-in-quartz data provide constraints on the temperature window (ΔT) of vein opening and deformation. In the deformed tonalite sample AD53, the reequilibrated quartz has a Ti signature identical to that in the recrystallized quartz in the adjacent quartz vein mylonite. This can be interpreted in two different ways: (i) the quartz in the vein was also Ti reequilibrated during deformation and recrystallization or (ii) the Ti content of quartz vein mylonite is inherited from the original Ti content of the vein. The fact that the WDV sample shows a similar but slightly higher Ti content than SDV indicates that, whatever the interpretation, the ΔT between vein opening and recrystallization was small, and up to 25°C at the most.

6.3. The CPO Evolution of the Adamello Quartz Veins

[39] We interpret that the lattice orientation of quartz crystals in the undeformed veins was not random but showed a CPO with a clear relationship to the kinematic framework during shearing. WDV include *c*-axis orientations distributed along a girdle inclined at a low angle to the vein boundary. The girdle includes a maximum at the periphery of the pole figure, at a relatively low angle to the lineation, and subordinate peaks parallel to *Y* and in symmetric intermediate orientations between the peripheral and *Y* maxima. This CPO type is unusual in quartzites but has been reported in garnet-bearing quartz tectonites deformed at upper amphibolite facies (685°–750°C) conditions [*Fernández et al.*, 2003]. It was interpreted as developing at high temperature due to the combined operation of prism ⟨c⟩, ⟨a⟩, and ⟨c+a⟩. In the Adamello area, the presence of this type of CPO within weakly deformed quartz veins suggests that it is not the result of plastic deformation. The Lobbia quartz veins opened during overall shearing as recorded by the local presence of quartz wings at the vein tips and the development of veins as dilational jogs [*Pennacchioni*, 2005]. Because of the relationship between the CPO and the kinematic framework in WDV, we speculate that the growth of crystals was sensitive to the imposed kinematics such that crystals well oriented for easy slip under the temperature conditions of deformation were favored to grow. The transition from dominant prism ⟨a⟩ to prism ⟨c⟩ slip is reported to occur at temperatures between 550°C [*Takeshita*, 1996] and >600°C [*Mainprice et al.*, 1986; *Stipp et al.*, 2002], and opening of the Lobbia veins may have occurred in this temperature range (580°C, assuming a_{TiO_2} = 0.4, for the WDV sample 09-174). Therefore, the WDV which show a CPO with a *c*-axis X maximum could be interpreted as evidence of an early stage of vein opening at a temperature high enough to promote prism ⟨c⟩ slip. If this assumption is correct, the CPO of samples 07-139D and 07-140, showing *c*-axis maxima close to both *Y* and X, could indicate crystal growth during opening at a slightly lower temperature than most of the WDV, together with a partial plastic overprint as indicated by the microstructure (Figure 2f). High-temperature, prism ⟨c⟩ slip has been recognized in granitic veins deformed during postmagmatic cooling [*Mainprice et al.*, 1986]. However, in the Lobbia quartz veins this interpretation does not explain why there are no corresponding "higher temperature" quartz mylonites that show a CPO with *c*-axis X maxima if prism ⟨c⟩ was active after vein formation. Actually, a higher temperature deformation in the WDV, than in MDV and SDV, is likely recorded by the presence of fast grain boundary migration recrystallization (GBM) microstructures (Figures 2d and 2e) and of coarser polygonization of grains (Figure 2f). GBM could have been promoted by the presence of abundant fluid inclusion in addition to the relatively high temperature. The phase of lower temperature deformation, probably coeval with the deformation in MDV and SDV, is probably witnessed in WDV by the development of small subgrains and new grains along discrete seams and conjugate microshear zones overprinting the coarse polygonization (Figures 2f). The MDV and SDV all show a Y maximum of *c* axis indicating the dominant activity of prism ⟨a⟩ slip, and Ti-in-quartz data indicate that opening and deformation of veins occurred in a small temperature window of about 25°C at most. The CPO typical of WDV is also present in MDV sample 07-157 (Figure 3) and as a local texture component (Figures 4 and 6) in some other MDV (e.g., samples 07-142 and AD03-05), but most MDV with $\gamma < 3$ show *c*-axis pole figures with partial *YZ* girdles, consistent with prism ⟨a⟩ and rhomb ⟨a⟩ slip. The dominant pole figure for MDV is almost indistinguishable from that of SDV and fits with the Y-maximum CPO expected for a deformation temperature >500°C [*Stipp et al.*, 2002].

[40] If MDV and SDV were derived from WDV, the development of the new CPO implies destruction of most of

Table 1. SIMS Data on Ti-in-Quartz with Temperatures Estimated from the Ti Content for Activities of TiO_2 of 1, 0.6, and 0.4

													a_{TiO2} = 1			a_{TiO2} = 0.6			a_{TiO2} = 0.4		
Sample_analysisID	Sample Type	*Offset*	*nA*	$^{48}Ti/^{30}Si$	$^{49}Ti/^{30}Si$	$^{40}Ca/^{30}Si$	$^{27}Al/^{30}Si$	$^{48}Ticorr$ (%)	SiO_2	^{48}Ti ppm	^{49}Ti ppm	Mean Ti	*T* (°C) (^{48}Ti)	*T*° (C) (^{49}Ti)	Mean T°C	T°C (^{48}Ti)	T°C (^{49}Ti)	Mean T°C	T°C (^{48}Ti)	T°C (^{49}Ti)	Mean T°C
AD53_01	Quartz vein (SDV)	*50*	*5*	0.0014	0.0016	0.0000	0.015	2	100	4.56	4.93		475	480		510	515		540	546	
AD53_02	Quartz vein (SDV)	*50*	*5*	0.0013	0.0013	0.0000	0.027	2	100	4.04	4.21		468	470		501	504		531	534	
AD53_03	Quartz vein (SDV)	*50*	*5*	0.0014	0.0014	0.0001	0.032	3	100	4.45	4.53		474	475		508	509		538	539	
AD53_04	Quartz vein (SDV)	*50*	*5*	0.0016	0.0016	0.0000	0.024	2	100	4.95	4.98		481	481		516	516		546	546	
AD53_05	Quartz vein (SDV)	*50*	*5*	0.0014	0.0015	0.0001	0.034	2	100	4.44	4.69	**4.6±0.3**	474	477	**475±5**	508	512	**510±5**	538	542	**540±6**
AD53_06	Tonalite mylonite	*50*	*5*	0.0013	0.0014	0.0001	0.025	3	100	4.24	4.32		471	472		505	506		534	536	
AD53_07	Tonalite mylonite	*50*	*5*	0.0042	0.0043	0.0000	0.008	1	100	13.36	13.57		552	553		594	595		631	632	
AD03-07_01	Quartz vein (SDV)	*50*	*5*	0.0018	0.0019	0.0001	0.084	2	100	5.84	5.97		492	493		528	529		559	561	
AD03-07_02	Quartz vein (SDV)	*50*	*5*	0.0021	0.0022	0.0000	0.011	1	100	6.70	7.13		501	505		538	543		570	575	
AD03-07_03	Quartz vein (SDV)	*50*	*5*	0.0020	0.0022	0.0000	0.007	1	100	6.42	6.83		498	502		535	539		567	572	
AD03-07_04	Quartz vein (SDV)	*50*	*5*	0.0019	0.0019	0.0000	0.013	1	100	6.08	6.10		494	495		531	531		562	562	
AD03-07_05	Quartz vein (SDV)	*50*	*5*	0.0020	0.0019	0.0001	0.082	2	100	6.22	6.14	**6.3±0.3**	496	495	**497±4**	533	532	**534±4**	564	563	**565±4**
AD07-174_01	Quartz vein (WDV)	*50*	*5*	0.0021	0.0021	0.0001	0.173	2	100	6.79	6.77		502	502		539	539		571	571	
AD07-174_02	Quartz vein (WDV)	*50*	*5*	0.0020	0.0020	0.0000	0.012	1	100	6.36	6.39		498	498		534	534		566	566	
AD07-174_03	Quartz vein (WDV)	*50*	*5*	0.0017	0.0017	0.0000	0.023	1	100	5.38	5.45		486	487		522	523		552	553	
AD07-174_04	Quartz vein (WDV)	*50*	*5*	0.0025	0.0025	0.0000	0.024	1	100	7.78	7.84		512	512		550	550		582	583	
AD07-174_05	Quartz vein (WDV)	*50*	*5*	0.0023	0.0024	0.0000	0.028	1	100	7.44	7.64		508	510		546	548		579	581	
AD07-174_06	Quartz vein (WDV)	*50*	*5*	0.0025	0.0024	0.0000	0.023	1	100	7.83	7.68		512	511		550	549		583	581	
AD07-174_07	Quartz vein (WDV)	*50*	*5*	0.0025	0.0025	0.0001	0.020	1	100	7.84	7.77		512	511		550	549		583	582	
AD07-174_08	Quartz vein (WDV)	*50*	*5*	0.0022	0.0022	0.0000	0.015	1	100	7.04	7.06	**7.1±0.9**	505	505	**504±9**	542	542	**548±4**	574	574	**580±4**
AD03-03A_01	Quartz vein (SDV)	*50*	*5*	0.0016	0.0016	0.0000	0.017	1	100	5.13	5.20		483	484		518	519		549	550	
AD03-03A_02	Quartz vein (SDV)	*50*	*5*	0.0018	0.0018	0.0000	0.017	1	100	5.73	5.74		490	491		526	527		557	558	
AD03-03A_03	Quartz vein (SDV)	*50*	*5*	0.0016	0.0016	0.0000	0.015	2	100	5.13	4.93		483	480		518	515		549	546	
AD03-03A_04	Quartz vein (SDV)	*50*	*5*	0.0019	0.0020	0.0000	0.015	1	100	5.88	6.21		492	496		528	532		560	564	
AD03-03A_05	Quartz vein (SDV)	*50*	*5*	0.0020	0.0021	0.0000	0.015	1	100	6.29	6.54	**5.7±0.5**	497	499	**490±6**	533	536	**525±7**	565	568	**556±7**
BOG1-Qz-32	Diff. grain loc.	*50*	*5*	0.0413	0.0412	0.0000	0.019	0	100	130.78	130.48		781	780		850	850		913	912	
BOG1-Qz-33	Near spot 06	*50*	*5*	0.0330	0.0331	0.0000	0.034	0	100	104.47	104.91		753	753		819	819		877	878	

the initial crystals and replacement by grains suitably oriented for prism ⟨a⟩ slip. The replacement process would have to have occurred pervasively at low strain and over a small strain range, before extensive recrystallization to fine aggregates, because MDV with less than 5% recrystallization already show a short YZ girdle for $\gamma \approx 2$. Fast grain boundary migration (GBM) recrystallization is potentially capable of producing such a textural change, with grains favorably oriented for prism ⟨a⟩ and rhomb ⟨a⟩ slip growing at the expense of original vein crystals oriented with their *c* axes at a low angle to the X direction. According to this hypothesis, original crystals poorly oriented for prism ⟨a⟩ slip would accumulate high dislocation density and be replaced by GBM [*Heilbronner and Tullis*, 2006]. GBM could explain the strongly serrated form and complex 3D intergrowth of crystals. In addition, recent experiments by *Muto et al*. [2009], made under conditions in which recrystallization occurs by subgrain rotation and rapid grain boundary migration, have shown that GBM can completely change an initial CPO. However, support for this interpretation is not very convincing for the following reasons: (i) many WDV do not contain a population of grains well oriented for prism ⟨a⟩ slip that could grow at the expense of the dominant population of poorly oriented crystals, (ii) the strain window for complete CPO replacement seems too small ($\gamma < 1$), and (iii) the CPO of WDV with a strong peripheral maximum close to the X axis is present in veins that do not show pervasive GBM microstructures (Figure 1a).

[41] A different interpretation of the texture evolution of the Lobbia quartz veins is that the WDV do not represent low strain remnants of the MDV and SDV but rather remnants of veins opened at a slightly higher temperature (if the interpretation that the kinematic framework controlled the growth orientation of vein crystals is correct). Early high-temperature veins, characterized by prism ⟨c⟩ orientations, might have been preserved from extensive deformation at lower temperature due to the unfavorably oriented CPO for prism ⟨a⟩ slip. Instead, veins formed at slightly lower temperature have a growth CPO dominated by *c* axes subparallel to Y (determined by the temperature of formation). There are exceptions and some veins include subordinate orientations of the other active, but less favorable, slip systems (rhomb and basal ⟨a⟩) or some local relict prism ⟨c⟩. The activity of rhomb and basal ⟨a⟩ slip during the main deformation is evident at the local scale (Figure 9). In this model, the ratio of the different quartz crystal orientations in the original veins (determined by the temperature of vein opening) controlled the strength of the vein. The absence of low-strain samples with a Y maximum of *c* axes can be explained by the fact that most of such veins were weak and easily underwent shearing. However, veins with a relatively high proportion of crystals initially well oriented for rhomb and basal ⟨a⟩ slip are less prone to accumulate strain, as in sample AD03-06. Similarly, both the CPO of the WDV (dominated by a near X maximum of *c* axes) and the CPO of the MDV and SDV (dominated by a Y maximum of *c* axes) were in an unfavorable orientation for slip at lower temperature (<500°C), where basal ⟨a⟩ slip should become dominant [*Stipp et al.*, 2002]. This explains why the Adamello veins were preserved from lower temperature reactivation during the later stages of pluton cooling, even though a stress field with the same regional orientation persisted throughout the whole cooling history of the Adamello tonalite down to $T \leq 250$°C. The maintenance of this same stress field during cooling of the pluton is evidenced by the identical kinematics of mylonitic shear zones and cataclastic faults developing in the tonalites with decreasing temperature, which exploit the same structural planes (joints and mylonites) [*Pennacchioni et al.*, 2006]. A similar sequence of postmagmatic joints, quartz veins, shear zones, and faults developing under an almost constant regional stress, as it is observed in the Adamello, has been recognized in other plutons (e.g., Lake Edison granodiorite Sierra Nevada, California; *Pennacchioni* [2009]).

[42] A similar interpretation of the control of CPO on the strength of quartzite at different temperatures was proposed by *Toy et al.* [2008] to account for the zoning in the CPO of quartz in mylonites and protomylonites in the hanging wall block of the Alpine Fault (New Zealand). They report a transition from a CPO with *c*-axis Y maxima and asymmetric single girdles in amphibolite facies mylonites in proximity to the Alpine Fault to crossed girdles in protomylonites further from the fault. The strong CPO of the amphibolite facies mylonites formed close to the main fault hindered their continued deformation during retrogression and favored the migration of the deformation to low strain domains where the fabric was weaker and therefore more prone to reactivation under lower temperature conditions where basal ⟨a⟩ slip was favored. The development of a CPO during plastic deformation therefore significantly modifies the strength of quartzites and, because of the strong temperature sensitivity of the slip systems in quartz, may act as a hardening mechanism in the case of constant kinematic axes with decreasing temperature.

[43] The resistance of quartz textures to later overprint, which is suggested to be uncommon in some cases [*Brunel*, 1980], should be common in ultramylonites where the CPO is strong and less important in protomylonites if the kinematic framework remains unchanged. The potentially different degree of texture reactivation of weakly and strongly strained rock makes the reconstruction of the CPO evolution with strain difficult.

6.4. Comparison of the Adamello Quartz Mylonites with Experiments

[44] The microstructural and textural evolution of quartzite during progressive shear has been investigated experimentally by *Heilbronner and Tullis* [2006] in the deformation regime where grain boundary migration and subgrain rotation recrystallization mechanisms were active. These experiments used the sample geometry introduced by *Dell'Angelo and Tullis* [1989], with a tabular slice of quartzite mounted between 45° precut pistons loaded axially in a Griggs apparatus. This setup can achieve high shear strains (up to $\gamma = 8$) under general shear conditions. It more closely simulates the simple shear deformation in the Adamello quartz veins than previous axial compression experiments on quartzites. Extrapolation of the experimental results of *Heilbronner and Tullis* [2006] to natural strain rates is consistent with the temperature regime of the Adamello quartz mylonites, and both experimental and natural examples develop similar types of pole figures in the recrystallized high strain mylonites. The experimental fabrics obtained by *Heilbronner and Tullis* [2006] can therefore be directly compared to the Adamello

microstructure and CPO, though there is a substantial difference in the starting material. In the experiments, the starting material was Black Hills quartzite, a fine-grained (about 100 μm in diameter), 99% pure quartzite with no deformation microstructures or *c*-axis CPO. In the Lobbia, the starting quartz veins consisted of coarse (millimeters to centimeters in size) crystals with a strong initial CPO. The main differences between the experimentally deformed quartzite and the natural mylonites are as follows:

[45] 1. In experiments, there is a continuous evolution of the CPO over a wide range of shear strain ($1 < \gamma < 8$), until complete recrystallization of the quartzite, whereas the CPOs in the Lobbia quartzites are present from the very first stages of shearing (and probably developed during vein growth), so recrystallized grains inherited the original CPO.

[46] 2. In experiments, the "final" Y-maximum-dominated pole figure of *c* axis is achieved only for complete recrystallization of the starting material to the fine steady-state grain size of 15 μm, whereas in the Lobbia quartz veins CPO development predates the extensive recrystallization to fine aggregates, and the CPO type and intensity appear to be strain insensitive, because they were present from the start.

[47] 3. In experiments, there is the development of a domainal fabric (domains with a different dominant CPO) and the domains, elongated in the foliation, have a size significantly larger than the starting grain size, whereas the domains of different CPO in the Lobbia quartz mylonites appear to correspond to original large vein crystals.

[48] In experiments, the CPO girdle rotates with increasing strain in a synthetic sense with regard to the sense of shear, whereas the CPO girdle of the Lobbia quartzites shows no significant and systematic rotation with γ.

[49] Most of these differences reflect the very different starting material in the experiments and the natural quartzites and the comparison provides information on the influence of initial grain size and of preexisting CPO on the fabric evolution of quartz veins. This must be taken into account when extrapolating experiments to natural quartz mylonites, which derive in most cases from deformation of original coarse-grained veins.

[50] There are also some features in common between experiments and the Adamello quartzites.

[51] 1. Basal ⟨a⟩, rhomb ⟨a⟩, and prism ⟨a⟩ slip systems were active at the same time though with a different degree of efficiency at $T > 500$°C. This information is partly obscured in the bulk CPO of the quartz mylonites but is clear at the local scale (e.g., Figure 9). In the case of the Adamello quartz veins it is difficult or impossible to establish if differences in the CPO of differently sheared samples are related to the different amount of accumulated strain or instead reflect differences in the initial growth CPO of vein crystals. However, because all SDV show textural domains and a CPO with a partial YZ girdle independent of the amount of strain, we suggest that the textural competition between the slip systems is almost negligible, in the recrystallized fine-grained aggregate up to very high strain.

[52] 2. The grain size of new grains remains constant regardless of the amount of total strain and, more importantly, of the amount of recrystallized material. Applying the piezometer of *Stipp and Tullis* [2003] to the Adamello quartz-mylonites, the grain size indicates a flow stresses of 35–40 MPa.

[53] A few large shear strain experiments in the dislocation creep regime have been performed on different geologically relevant minerals using the Paterson torsion apparatus: calcite [*Casey et al.*, 1998; *Pieri et al.*, 2001, *Barnhoorn et al.*, 2004], olivine [*Bystricky et al.*, 2000], anhydrite [*Heidelbach et al.*, 2001], halite [*Wenk et al.*, 2009], gypsum [*Barberini et al.*, 2005], and Mg-wüstite [*Heidelbach et al.*, 2003]. Though these experimental data form a restricted database and refer to totally different minerals, they yield some consistent information.

[54] 1. Recrystallization occurs gradually over a relatively large range of shear strain ($\Delta\gamma$). For high-*T* experiments on calcite, $\Delta\gamma$ is 9.2 and 4.4 from incipient to complete and pervasive (75%) recrystallization, respectively; the stage of recrystallization closely matches with mechanical weakening after peak stress. For olivine, $\Delta\gamma$ is 5.5 and largely outlasts the stage of mechanical weakening. For halite $\Delta\gamma$ is 5. For gypsum, there is significant recrystallization for $\Delta\gamma = 1$, but the data are incomplete and approximate. For anhydrite, microstructural descriptions are missing.

[55] 2. The CPO continuously evolves with increasing strain, progressively changing orientation and strength. In calcite there is a change in pole figure type at low strain, resulting finally in an almost steady-state CPO for $\gamma > 5$ in high-*T* experiments. However, there is a continuous strengthening of the CPO until very large strain, and the pattern progressively approaches orthorhombic asymmetry. In olivine, there is also a gradual change in CPO type during recrystallization and the texture becomes much stronger and symmetric at high strain.

[56] These general observations are in line with what was observed in the quartzite experiments of *Heilbronner and Tullis* [2006]. All the experiments used fine-grained, initially texture-free, material. A main difference between the torsion experiments and those of *Heilbronner and Tullis* [2006] is that, in these latter, the CPO asymmetry tends to increase with increasing strain. This difference could reflect the fairly strong thinning component of the general shear involved in the experiments of *Heilbronner and Tullis* [2006], which is almost absent in the experiments with a rotary Paterson apparatus and in the sheared Lobbia veins, where deformation approached simple shear.

[57] If the data of our study can be generalized, the extrapolation of these experimental results to natural quartz aggregates derived from shearing of coarse-grained veins is limited. For example the same final CPO in veins can be achieved at much lower strains in natural quartz mylonites than in experiments.

6.5. Domainal CPO Development

[58] Under crossed polars, all the Adamello quartz mylonites show a clear domainal extinction with domains elongated to define the foliation. A domainal texture is characteristic of many quartz mylonites [e.g. *Wilson*, 1975; *Bouchez*, 1977; *Law et al.,* 1990; *Knipe and Law*, 1987; *Pauli et al.*, 1996; *Mancktelow and Pennacchioni*, 2004] and persists as a fabric element up to high strain.

[59] We show in this study that, due to the domainal fabric of most of the quartz mylonites, the CPO is dependent on the original grain size and, below a certain size, the variability of local CPO spans the whole range from a single girdle to a strong Y maximum. This domainal fabric persists

with complete recrystallization and to the largest recorded strains. The CPO variability does not reflect a change in temperature, but the original presence of different quartz orientations in the veins. The local scale variability of CPO in a quartz mylonite associated with a strong strain partitioning has been well illustrated by *Pauli et al.* [1996]. Also in their case [as in *Stipp et al.*, 2002, and in the current study], the quartz mylonites developed from initially coarse-grained veins. In the case of the Adamello quartz mylonites, a uniform CPO is found only for areas relatively large enough to encompass a significant portion of the domainal fabric. At this scale, the CPO of most samples is consistent with the reference scheme of *Stipp et al.* [2002] for the synkinematic conditions of deformation (i.e., slightly above 500°C) but with significant exceptions (sample AD03-06).

7. Conclusions

[60] Coarse-grained quartz veins opened and were deformed by simple shear to various shear strains over a small temperature window (<25°C), within the range 500°C to 580°C, during postmagmatic cooling of the Adamello pluton. The sheared veins show three different types of microstructures and CPOs: (a) weakly deformed veins (WDV: $\gamma < 1$), (b) moderately deformed veins (MDV: $2 < \gamma < 3$), and (c) strongly deformed veins (SDV: $\gamma = 4$ to 15). The veins appear to have developed with an initial strong growth CPO. The WDV are coarse grained and show a growth CPO with the *c* axes forming a girdle at a small angle to the vein wall and with a strong *c*-axis maximum close to lineation. This CPO was preserved in the WDV during subsequent (lower temperature) limited plastic deformation, which occurs in the field of dominant prism ⟨a⟩ slip. Veins where the quartz crystals developed an initial growth CPO with a *c*-axis Y maximum were in contrast able to easily deform and developed into MDV and SDV. The amount of accumulated strain was determined in part by proportion of initial crystals in the vein that were well oriented for prism ⟨a⟩ slip. We believe that, given the relation of the CPO to the kinematic axes, the vein crystals grew in an orientation for easy slip that was determined by the temperature during growth. Given the small temperature window for vein opening and ductile deformation (about 25°C), the range in temperature probably overlapped the temperature boundary corresponding to the switch from prism ⟨c⟩ slip to prism ⟨a⟩ slip.

[61] The MDV consist of elongate coarse grains defining the foliation, with only minor fine recrystallization, and show a strong CPO with the *c* axes forming a partial YZ girdle. Recrystallization occurred abruptly in a small γ range between 2 and 3 and did not significantly alter the CPO. SDV are almost completely finely recrystallized and have a strong CPO similar to that of MDV. The CPO of MDV and SDV is consistent with prism ⟨a⟩ and subordinate rhomb ⟨a⟩ slip. The microstructure and CPO of most SDV achieved steady state, as there is no variation of grain size and CPO strength or type with increasing shear strain from $\gamma \sim 3$ to 15. On the other hand, original differences in the vein crystal orientations were maintained up to high strain in the form of textural banding. The achievement of a bulk steady-state fabric early in the deformation history, in comparison with many experimental results, is favored by the preexisting growth CPO. At the same time, initial crystal orientations in the vein that were well oriented for glide on secondary slip systems (rhomb ⟨a⟩ and basal ⟨a⟩) at the deformation temperatures persist up to high shear strains. The original CPO of the veins strongly influenced the strength of the veins during subsequent deformation and prevented the high-temperature fabric from being reworked at lower temperature. The CPO of WDV and MDV-SDV are all badly oriented for basal ⟨a⟩ slip.

[62] These interpretations apply to plastic deformation of coarse-grained veins. There are many points, however, that needs to be understood or clarified or proved in future studies: (i) the mechanism of the inferred development of a strong growth CPO within quartz veins controlled by the temperature of opening and (ii) the reason for the occurrence of recrystallization in a small range of γ, which is in contrasts with the observation in some experiments and other natural quartz mylonites. To solve these problems and to extrapolate the conclusions of this paper to other mylonites, there is the need of other studies on sheared quartz veins, where the microstructural and CPO evolution can be correlated to measured strains and where strain geometry and ambient conditions of deformation are well constrained.

Appendix A: Techniques of Measurement of Crystallographic Preferred Orientation, X-ray Texture Goniometry

[63] The pole-figure measurements for quantitative texture analysis were carried out on a PANalytical X-ray texture measuring system installed at the Geoscience Centre of the University of Göttingen, Germany [*Leiss*, 2005; *Leiss and Ullemeyer*, 2006]. A poly-capillary glass fiber lens at the primary beam side provides high X-ray intensities, an optically parallel beam, and an exceptionally large beam size of up to 7 mm. This allows a short measuring time per pole figure (1 s per pole-figure direction at an anode current of 40 mA and a voltage of 40 kV), a high resolution, and a relative large measured volume. Computer-controlled sample movement allows automated measurements of a series of local textures on a regular or irregular grid within a polished sample area of 100 × 100 mm. This provides a control on the texture homogeneity of the sample texture and/or improves the measuring statistics especially for coarse-grained samples by accumulating several pole-figure measurements into a bulk pole figure. In the case of the coarse-grained WDV and MDV samples, we accumulated up to six local texture measurements to establish a representative global texture of the samples. A standard pole-figure measuring grid of 5° × 5° was applied for quartz (100), (101), (110), (102), (111), (200), (201), (112), (211) and for background measurement. After subtraction of the background from the quartz measurements, a defocusing correction based on functions derived from pole-figure measurements of quartz powder [e.g., *Wassermann and Grewen*, 1962; *Wenk*, 1985] was carried out. At high tilt angles, reasonable defocusing corrections are not possible, therefore measurements were cut off at a tilt angle of 85°, leading to incomplete pole figures. The orientation distribution function (ODF) values in three-dimensional orientation space were calculated by

means of the WIMV algorithm [*Matthies and Vinel*, 1982], included in the BEARTEX software package [*Wenk et al.*, 1998]. From the results of the ODF, full pole figures and pole figures that cannot be directly measured, such as quartz (001) (*c* axis), were calculated.

Appendix B: Techniques of Measurement of Crystallographic Preferred Orientation, Computer Integrated Polarization Microscopy

[64] The photomicrographs used to derive the CIP pole figures were acquired with a Zeiss AxioCam MRm digital camera on a Zeiss Axioplan microscope. Images are oriented with the top and bottom edges parallel to the shear zone boundaries (XY plane of the bulk finite strain). For all CIP analyses, a magnification of 2.5 × was used. With this setup, the pixel size is 6 μm^2 and the area of individual regions of interest ranges from 4 to 7 mm^2 (0.7 to 1.2 megapixels). This is quite a small area of the thin section, especially considering the relatively coarse grain size of the WDV and the domainal fabric of the SDV. Therefore, in order to obtain meaningful information, using CIP analysis the CPO was measured in at least six domains per sample, corresponding to a total investigated area in the range of 35 to 40 mm^2. The main goal of the CIP analysis was not to represent the bulk texture but to understand the texture of particular microstructural domains; the local CIP texture analysis is complementary to the bulk texture analysis with X-ray texture goniometry. For example, *c*-axis orientations were determined for different textural domains defining the foliation.

[65] The CIP analysis estimates the *c*-axis orientation at each pixel of the image and derives (i) area-weighted pole figures and (ii) *c*-axis orientation images (COI) according to two-dimensional color look-up tables (CLUTs). For each measured domain the bulk pole figure was calculated. In addition, for some samples of WDV and MDV we derived partial pole figures of the recrystallized grains separately. The *c*-axis orientation images were visualized by means of a spectrum CLUT that represents the Z direction in blue, the X direction in yellow, and the Y direction in white. For the SDV we also used an alternative CLUT to highlight specific orientation domains, following the procedure of *Heilbronner and Tullis* [2006]. Specifically, blue pixels represent grains suitably oriented for basal ⟨a⟩, pink grains have orientations suitable for rhomb ⟨a⟩ slip, and white grains for prism ⟨a⟩ slip. Green pixels have the *c*-axis subparallel to the maximum compression direction and are therefore unsuitably oriented for ⟨a⟩ slip, whereas yellow pixels do not fall into any of these domains.

Appendix C: Ti Measurement and Titanium-in-Quartz Thermometry

[66] The Ti concentration in quartz was determined by SIMS (Cameca IMS 4f) at the EIMF, University of Edinburgh, in four samples (1 WDV: AD07-174; 3 SDV: AD03-03A, AD03-07, and AD53), with the aim of applying the Ti-in-quartz thermometer calibrated by *Wark and Watson* [2006]. The thermometer has been calibrated for a relatively high temperature range (600°–1000°C), in the presence of rutile, although it might be also applicable to lower temperature mylonites [*Kohn and Northrup*, 2009; *Grujic et al.*, 2009].

[67] The mylonitic quartzite sample AD53 was studied by *Pennacchioni* [2005] and its CPO, determined by texture goniometer, includes a strong *c*-axis Y maximum [see figure 8 of *Pennacchioni*, 2005], as for most of the SDV. This sample was chosen because it also contains a tonalite mylonite, adjacent to the quartz mylonite. The Ti content of deformed and recrystallized magmatic quartz in the tonalite mylonite grains was measured for comparison with the Ti in the associated mylonitic quartz vein. The matrix of the tonalite mylonite includes abundant ilmenite derived from recrystallization of the Ti-rich magmatic biotite, which provides a buffer for the Ti content in quartz. In contrast, the quartz veins do not contain rutile or other Ti-bearing minerals.

[68] Gold-coated polished samples were sputtered with a 5 nA ^{16}O beam accelerated to 10 kV and positive secondary ions (accelerated to 4.5 kV at 50 V offset with an energy window of 25 V) were collected. The spot size was approximately 20 × 25 μm (i.e., smaller than the mean grain size of recrystallized quartzites). We analyzed masses of ^{26}Mg, ^{27}Al, ^{30}Si, ^{40}Ca, ^{44}Ca, ^{48}Ti, and ^{49}Ti in low-mass resolution with total counting time of 500 s for each isotope divided over 10 cycles, except for ^{30}Si (200 s) and ^{49}Ti (1000 s).

[69] The ^{48}Ti signal needed to be corrected for isotopic overlap of ^{48}Ca and molecular interferences of $^{30}Si^{18}O$ and ^{24}Mg. The contribution of the latter is negligible in quartz, but $^{30}Si^{18}O$ was significant and was calculated from $^{28}Si^{16}O$ (on mass 44) after subtraction of ^{44}Ca using a modified $^{16}O/^{18}O$ ratio of 1500 to adjust for ^{16}O enrichment of the sample surface due to ^{16}O implantation by the primary ion beam [*Hinton*, 1995]. The total contribution of ^{48}Ca and $^{30}Si^{18}O$ amounted to no more than 4% of the ^{48}Ti signal in the samples presented here, which converts to an equivalent Ti concentration of 0.1–0.2 ppm. The corrected $^{48}Ti/^{49}Ti$ ratio was close to the expected natural abundance ratio of 13.4, which confirms the accuracy of the corrections, even for standard material SRM610 (see below), despite a much larger correction for ^{48}Ca (ca. 40% of ^{48}Ti signal). The agreement between the two Ti isotopes also indicates that no unexpected interferences were present in either signal.

[70] ^{27}Al and ^{40}Ca were used to monitor for surface contamination or small invisible inclusions in quartz. Both elements showed significant grain-to-grain variability, while ^{40}Ca usually decreased gradually during analysis, indicative of surface contamination. Ti signals, however, were constant and independent of Al and Ca levels.

[71] Ti contents were calculated from corrected $^{48}Ti/^{30}Si$ and $^{49}Ti/^{30}Si$ signal ratios and known SiO_2 contents of samples and the calibration standard. We used NIST SRM610 glass (Ti = 434 ppm) [*Pearce et al.,* 1997] as a standard, due to the lack of a suitable quartz standard with known Ti content. This approach assumes that the relative ion yield of Ti in quartz and SRM610 glass (a Na-Ca-Al silicate glass doped with trace elements) is the same and thus independent of sample matrix. Although we cannot prove the validity of this assumption, the following observations suggest its validity: (i) virtually no change in measured Ti content was observed after changing the energy offset from 50 to 120 V and (ii) little matrix-dependent fractionation was observed relative to NIST SRM610 glass for Ti in

olivine [*De Hoog et al.,* 2010] and zircon (EIMF, unpublished data). Even if a small matrix effect affected the results, a deviation of the measured value from the true value of 20% would result in a temperature bias of less than 15°C and would therefore not alter the conclusions of this paper.

[72] **Acknowledgments.** This study has been funded by Fondazione Cariparo (Progetti di eccellenza, 2008). Renee Heilbronner is thanked for teaching the fundamentals of image analysis, as well as for providing the facilities for CIP analysis. Cees-Jan De Hoog is thanked for assistance in measuring Ti in quartz at the EIMF. Neil S. Mancktelow is thanked for reading the manuscript before submission and suggesting substantial improvements. Reviews by Virginia Toy and 2 anonymous reviewers helped greatly to improve the final version of the manuscript. The X-ray texture goniometer was financed by the Volkswagen Foundation.

References

Barberini, V., L. Burlini, E. H. Rutter, and M. Dapiaggi (2005), High-strain deformation tests on natural gypsum aggregates in torsion, in *High-Strain Zones: Structure and Physical Properties*, *Geol. Soc. London Spec. Publ. 245*, edited by D. Bruhn and L. Burlini, pp. 277–290.

Barnhoorn, A., M. Bystricky, L. Burlini, and K. Kunze (2004), The role of recrystallisation on the deformation behaviour of calcite rocks: Large strain torsion experiments on Carrara marble, *J. Struct. Geol.*, *26*(5), 885–903, doi:10.1016/j.jsg.2003.11.024.

Bouchez, J. L. (1977), Plastic-deformation of quartzites at low-temperature in an area of natural strain gradient, *Tectonophysics*, *39* (1–3), 25–50.

Brodie, K. H., and E. H. Rutter (2000), Deformation mechanisms and rheology: Why marble is weaker than quartzite, *J. Geol. Soc. London*, *157*(6), 1093–1096.

Brunel, M. (1980), Quartz fabrics in shear-zone mylonites: Evidence for a major imprint due to late strain increments, *Tectonophysics*, *64*(3–4), T33–T44, doi:10.1016/0040-1951(80)90094-3.

Burg, J.-P., and P. H. Laurent (1978), Strain analysis of a shear zone in a granodiorite, *Tectonophysics*, *47*(1–2), 15–42, doi:10.1016/0040-1951(78)90149-X.

Bystricky, M., K. Kunze, L. Burlini, and J.-P. Burg (2000), High shear strain of olivine aggregates: Rheological and seismic consequences, *Science*, *290*, 1564–1567, doi: 10.1126/science.290.5496.1564.

Carreras, J., and A. Garcia Celma (1982), Quartz *c*-axis fabric variation at the margins of a shear zone developed in schists from Cap de Creus (Spain), *Acta Geol. Hisp.*, *17*(3), 137–149.

Casey, M., K. Kunze, and D. L. Olgaard (1998), Texture of Solnhofen limestone deformed to high strains in torsion, *J. Struct. Geol.*, *20*(2–3), 255–267, doi:10.1016/S0191-8141(97)00058-8.

De Hoog, J. C. M., L. Gall, and D. H. Cornell (2010), Trace element geochemistry of mantle olivine and applications to mantle petrogenesis and geothermobarometry, *Chem. Geol.*, *270*(1–4), 196–215, doi:10.1016/j.chemgeo.2009.11.017.

Dell'Angelo, L., and J. Tullis (1989), Fabric development in experimentally sheared quartzites, *Tectonophysics*, *169*(1–3), 1–21, doi:10.1016/0040-1951(89)90180-7.

Fernández, F. J., H. I. Chaminé, P. E. Fonseca, J. M. Munhá, A. Ribeiro, J. Aller, M. Fuertes-Fuentes, and F. S. Borges (2003), HT-fabrics in a garnet-bearing quartzite from Western Portugal: geodynamic implications for the Iberian Variscan Belt, *Terra Nova*, *15*(2), 96–103, doi:10.1046/j.1365-3121.2003.00472.x.

Gleason, G. C., and J. Tullis (1995), A flow law for dislocation creep of quartz aggregates determined with the molten-salt cell, *Tectonophysics*, *247*(1–4), 1–23, doi:10.1016/0040-1951(95)00011-B.

Grujic, D., M. Stipp, and J. L. Wooden (2009), Thermometry of quartz mylonites, *Geochim. Cosmochim. Acta*, *73*(13), Supplement 1, A472–A472, doi:10.1016/j.gca.2009.05.025.

Hara, I., K. Takeda, and T. Kimura, T. (1973), Preferred lattice orientation of quartz in shear deformation, *J. Science Hiroshima Uni., Serie C*, *7*, 1–11.

Heidelbach, F., I. C. Stretton, and K. Kunze (2001), Texture development of polycrystalline anhydrite experimentally deformed in torsion, *Int. J. Earth Sci. (Geol. Rundsch.)*, *90*(1), 118–126, doi:10.1007/s005310000162.

Heidelbach, F., I. Stretton, F. Langenhorst, and S. Mackwell (2003), Fabric evolution during high shear strain deformation of magnesiowüstite ($Mg_{0.8}Fe_{0.2}O$), *J. Geophys. Res.*, *108*(B3), 2154, doi:10.1029/2001JB001632.

Heilbronner, R. (2000), Optical orientation imaging, in: *Stress, Strain and Structure, a Volume in Honour of W.D. Means*, edited by M. W. Jessel and J. L. Urai, *J. Virtual Explorer*, *2*, <http://virtualexplorer.com.au/VEjournal/Volume 2/>.

Heilbronner, R., and J. Tullis (2002), The effect of static annealing on microstructure and crystallographic preferred orientations of quartzites experimentally deformed in axial compression and shear, in *Deformation Mechanisms, Rheology and Tectonics: Current Status and Future Perspectives*, *Geol. Soc. Special Publ.*, vol. 200, edited by S. de Meer et al., pp. 191–218.

Heilbronner, R., and J. Tullis (2006), Evolution of *c*-axis pole figures and grain size during dynamic recrystallization: Results from experimentally sheared quartzite, *J. Geophys. Res.*, *111*, B10202, doi:10.1029/2005JB004194.

Hinton, R. W. (1995), Ion microprobe analysis in geology, in *Microprobe techniques in the earth sciences*, *Mineral. Soc. Series*, vol. 6, edited by P. J. Potts et al., pp. 235–290, Chapman & Hall, London, UK.

Hirth, G., C. Teyssier, and W. J. Dunlap (2001), An evaluation of quartzite flow laws based on comparison between experimentally and naturally deformed rocks, *Int. J. Earth Sci. (Geol. Rundsch.)*, *90*(1), 77–87, doi:10.1007/s005310000152.

Hirth, G., and J. Tullis (1992), Dislocation creep regimes in quartz aggregates, *J. Struct. Geol.*, *14*(2), 145–159, doi:10.1016/0191-8141(92)90053-Y.

John, B. E., and J. D. Blundy (1993), Emplacement-related deformation of granitoid magmas, southern Adamello Massif, Italy, *Geol. Soc. Am. Bull.*, *105*, 1517–1541.

Knipe, R. J., and R. D. Law (1987), The influence of crystallographic orientation and grain boundary migration on microstructural and textural evolution in an S-C mylonite, *Tectonophysics*, *135*(1–3), 155–169.

Kohn, J. K, and C. J. Northrup (2009), Taking mylonites' temperatures, *Geology*, *37*(1), 47–50, doi:10.1130/G25081A.1.

Kronenberg, A. K., and J. Tullis (1984), Flow strengths of quartz aggregates: Grain size and pressure effects due to hydrolytic weakening, *J. Geophys. Res.*, *89*(B6), 4281–4297, doi:10.1029/JB089iB06p04281.

Law, R. D., S. M. Schmid, and J. Wheeler (1990), Simple shear deformation and quartz crystallographic fabrics: A possible natural example from the Torrion area of NW Scotland, *J. Struct. Geol.*, *12*(1), 29–45, doi:10.1016/0191-8141(90)90046-2.

Leiss, B. (2005), New techniques, measuring strategies and applications of conventional X-ray texture analysis, Conference abstracts 'Deformation Mechanism, Rheology and Tectonics', Zurich, Switzerland.

Leiss, B., and K. Ullemeyer (2006), Neue Perspektiven der Texturanalytik von Gesteinen mit konventioneller Röntgenbeugung, in: *Symposium "Tektonik, Struktur und Kristallingeologie,"* edited by S. L. Philipp et al., Universitätsverlag Göttingen, 128–130.

Lister, G. S., and M. S. Paterson (1979), The simulation of fabric development during plastic deformation and its application to quartzite: Fabric transitions, *J. Struct. Geol.*, *1*(2), 99–115, doi:10.1016/0191-8141(79)90047-6.

Lloyd, G. E., R. D. Law, D. Mainprice, and J. Wheeler (1992), Microstructural and crystal fabric evolution during shear zone formation, *J. Struct. Geol.*, *14*(8–9), 1079–1100, doi:10.1016/0191-8141(92)90037-W.

Mainprice, D. H., J.-L. Bouches, P. Blumenfeld, and J. M. Tubiá (1986), Dominant c slip in naturally deformed quartz: implications for dramatic plastic softening at high temperature, *Geology*, *14*(10), 819–822, doi:10.1130/0091-7613(1986)14<819:DCSIND>2.0.CO;2.

Mancktelow, N. S., and G. Pennacchioni (2004), The influence of grain boundary fluids on the microstructure of quartz-feldspar mylonites, *J. Struct. Geol.*, *26*(1), 47–69, doi:10.1016/S0191-8141(03)00081-6.

Mancktelow, N. S., and G. Pennacchioni (2005), The control of precursor brittle fracture and fluid–rock interaction on the development of single and paired ductile shear zones, *J. Struct. Geol.*, *27*, 645–661, doi:10.1016/j.jsg.2004.12.001.

Mancktelow, N. S., and G. Pennacchioni (2010), Why calcite can be stronger than quartz, *J. Geophys. Res.*, *115*, B01402, doi:10.1029/2009JB006526

Matthies, S., and G. W. Vinel (1982), An example demonstrating a new reproduction method of the ODF of texturized samples from pole figures, *Phys. Status Solidi(b)*, *112*(2), K115–K120, doi:10.1002/pssb.2221120255.

Menegon, L., G. Pennacchioni, R. Heilbronner, and L. Pittarello (2008), Evolution of quartz microstructure and *c*-axis crystallographic preferred orientation within ductilely deformed granitoids (Arolla Unit, Western Alps), *J. Struct. Geol.*, *30*(11), 1332–1347, doi:10.1016/j.jsg.2008.07.007.

Mittempergher, S., G. Pennacchioni, and G. Di Toro (2009), The effects of fault orientation and fluid infiltration on fault rock assemblages at seis-

mogenic depths, *J. Struct. Geol.*, *31*(12), 1511–1524, doi:10.1016/j.jsg.2009.09.003.

Muto, J., G. Hirth, R. Heilbronner, and J. Tullis (2009), Plastic anisotropy and LPO development in sheared and recrystallized quartz single crystals, *Eos Trans. AGU*, *90*(52), *Fall Meet. Suppl.*, Abstract MR14A-03.

Oesterling, N., R. Heilbronner, H. Stünitz, A. Barnhoorn, and G. Molli (2007), Strain dependent variation of microstructure and texture in naturally deformed Carrara marble, *J. Struct. Geol.*, *29* (4), 681–696, doi:10.1016/j.jsg.2006.10.007.

Panozzo Heilbronner, R., and C. Pauli (1993), Integrated spatial and orientation analysis of quartz *c*-axes by computer-aided microscopy, *J. Struct. Geol.*, *15*(3–5), 369–382, doi:10.1016/0191-8141(93)90133-U.

Paterson, M. S., and F. C. Luan (1990), Quartzite rheology under geological conditions, in *Deformation Mechanisms, Rheology and Tectonics*, *Geol. Soc. Spec. Publ.*, vol. 54, edited by R. J. Knipe and E. H. Rutter, pp. 299–307.

Pauli, C., S. M. Schmid, and R. Panozzo Heilbronner (1996), Fabric domains in quartz mylonites: localized three dimensional analysis of microstructure and texture, *J. Struct. Geol.*, *18*(10), 1183–1203, doi:10.1016/S0191-8141(96)00017-X.

Pearce, N. J. G., W. T. Perkins, J. A. Westgate, M. P. Gorton, S. E. Jackson, C. R. Neal, and S. P. Chenery (1997), A compilation of new and published major and trace element data for NIST SRM 610 and NIST SRM 612 glass reference materials, *Geostand. Geoanal. Res.*, *21*(1), 115–144, doi:10.1111/j.1751-908X.1997.tb00538.x.

Pennacchioni, G. (2005), Control of the geometry of precursor brittle structures on the type of ductile shear zone in the Adamello tonalites, Southern Alps (Italy), *J. Struct. Geol.*, *27*(4), 627–644, doi:10.1016/j.jsg.2004.11.008.

Pennacchioni, G. (2009), High temperature solid-state coeval brittle and ductile deformation during cooling of Lake Edison Granodiorite (Sierra Nevada, California), *Eos Trans. AGU*, *90*(52), *Fall Meet. Suppl.*, Abstract T32C-08.

Pennacchioni, G., G. Di Toro, P. Brack, L. Menegon, and I. M. Villa (2006), Brittle-ductile-brittle deformation during cooling of tonalite (Adamello, Southern Italian Alps), *Tectonophysics*, *247*(1–4), 171–197, doi:10.1016/j.tecto.2006.05.019.

Pennacchioni, G., and N. S. Mancktelow (2007), Nucleation and initial growth of a shear zone network within compositionally and structurally heterogeneous granitoids under amphibolite facies conditions, *J. Struct. Geol.*, *29*(11), 1757–1780, doi:10.1016/j.jsg.2007.06.002.

Pieri, M., L. Burlini, K. Kunze, I. Stretton, and D. L. Olgaard (2001), Rheological and microstructural evolution of Carrara marble with high shear strain: Results from high temperature torsion experiments, *J. Struct. Geol.*, *23*(9), 1393–1413, doi:10.1016/S0191-8141(01)00006-2.

Ramsay, J. G. (1980), Shear zone geometry: A review, *J. Struct. Geol.*, *2*(1–2), 83–99, doi:10.1016/0191-8141(80)90038-3.

Regenauer-Lieb, K., R. F. Weinberg, and G. Rosenbaum (2006), The effect of energy feedbacks on continental strength, *Nature*, *442*, 67–70, doi:10.1038/nature04868.

Rutter, E. H., and K. H. Brodie (2004), Experimental intracrystalline plastic flow in hot-pressed synthetic quartzite prepared from Brazilian quartz crystals, *J. Struct. Geol.*, *26* (2), 259–270, doi:10.1016/S0191-8141(03)00096-8.

Sander, B. (1950), *Einführung in die Gefügekunde der geologischen Körper. Band II: Die Korngefüge*, Springer-Verlag, Berlin.

Schmid, S. M., and M. Casey (1986), Complete fabric analysis of some commonly observed quartz *c*-axis patterns: Mineral and rock deformation, *AGU Geophys. Monogr.*, *36*, 263–286.

Schmocker, M. (2002), Rheology and Microfabrics of Quartz: Experimental Deformation in Torsion, PhD thesis, Diss. ETH Nr. 14587, ETH Zürich, Switzerland.

Schmocker, M., M. Bystricky, K. Kunze, and L. Burlini (2003), Granular flow and Riedel band formation in water-rich quartz aggregates experimentally deformed in torsion, *J. Geophys. Res.*, *108*(B5), 2242, doi:10.1029/2002JB001958.

Simpson, C. (1980), Oblique girdle orientation patterns of quartz *c*-axes from a shear zone in the basement core of the Maggia Nappe Ticino, Switzerland, *J. Struct. Geol.*, *2*(1–2), 243–247, doi:10.1016/0191-8141(80)90056-5

Stipp, M., H. Stünitz, R. Heilbronner, and S. M. Schmid (2002), The Eastern Tonale fault zone: A "natural laboratory" for crystal plastic deformation of quartz over a temperature range from 250°C to 700°C, *J. Struct. Geol.*, *24*(12), 1861–1884, doi:10.1016/S0191-8141(02)00035-4.

Stipp, M., and J. Tullis (2003), The recrystallized grain size piezometer for quartz, *Geophys. Res. Lett.*, *30*(21), 2088, doi:10.1029/2003GL018444.

Takeshita, T. (1996), Estimate of physical conditions for deformation based on *c*-axis transitions in naturally deformed quartzite, *J. Geol. Soc. Jpn.*, *102*, 211–222.

Toussaint, G., E. Burov, and J.-P. Avouac (2004), Tectonic evolution of a continental collision zone: A thermomechanical numerical model, *Tectonics*, *23*, TC6003, doi:10.1029/2003TC001604.

Toy, V. G., D. J. Prior, and R. J. Norris (2008), Quartz fabrics in the Alpine Fault mylonites: Influence of pre-existing preferred orientations on fabric development during progressive uplift, *J. Struct. Geol.*, *30*(5), 602–621, doi:10.1016/j.jsg.2008.01.001.

Trommsdorff, V., and H. R. Wenk (1963), Diskussion eines Zwillingsgefüges durch Achsenverteilungsanalyse an Quarz eines Tessiner Gneisses, *Schweiz. Mineral. Petrog. Mitt.*, *43*, 687–698.

Tullis, J., and R. A. Yund (1989), Hydrolytic weakening of quartz aggregates: The effects of water and pressure on recovery, *Geophys. Res. Lett.*, *16*(11), 1343–1346, doi:10.1029/GL016i011p01343.

van Roermund, H., G. S. Lister, and P. F. Williams (1979), Progressive development of quartz fabrics in a shear zone from Monte Mucrone, Sesia-Lanzo Zone, Italian Alps, *J. Struct. Geol.*, *1*(1), 43–52, doi:10.1016/0191-8141(79)90020-8.

Wark, D. A., and E. B. Watson (2006), TitaniQ: a titanium-in-quartz geothermometer, *Contrib. Mineral. Petrol.*, *152*(6), 743–754, doi:10.1007/s00410-006-0132-1.

Wassermann, G., and J. Grewen (1962), *Texturen metallischer Werkstoffe*, Springer-Verlag, Berlin.

Wenk, H. R. (1985), *Preferred orientation in deformed metals and rocks: An introduction to modern texture analysis*, Academic Press, Orlando, Florida.

Wenk, H. R., S. Matthies, J. Donovan, and D. Chateigner (1998), BEARTEX: a Windows-based program system for quantitative texture analysis, *J. Appl. Crystallogr.*, *31*(2), 262–269, doi: 10.1107/S002188989700811X.

Wenk, H.-R., M. Armann, L. Burlini, K. Kunze, and M. Bortolotti (2009), Large strain shearing of halite: Experimental and theoretical evidence for dynamic texture changes, *Earth Planet. Sci. Lett.*, *280*(1–4), 205–210, doi:10.1016/j.epsl.2007.09.018.

Werling, E. (1992), Tonale-, Pejo- und Judicarien-Linie: Kinematik, Mikrostrukturen und Metamorphose von Tectoniten aus räumlich interferierenden aber verschiedenaltrigen Verwerfungszonen, PhD thesis, ETH Zürich, Switzerland, 276 pp.

Wilson, C. J. L. (1975), Preferred orientation in quartz ribbon mylonites, *Geol. Soc. Am. Bull.*, Jul; *86*(7), 968–974.

F. Nestola and G. Pennacchioni, Dipartimento di Geoscienze, University of Padova, Via Grandenigo 6, I-35131 Padova, Italy. (giorgio.pennacchioni@unipd.it)

L. Menegon, Institutt for geologi, Universitetet i Tromsø, Dramsveien 201, N-9037 Tromsø, Norway.

B. Leiss, Geowissenschaftliches Zentrum, Universität Göttingen (GZG), Goldschmidtstr. 3, D-37077 Göttingen, Germany.

G. Bromiley, School of GeoSciences, University of Edinburgh, Grant Institute, King's Buildings, West Main Rd, Edinburgh EH9 3JW, United Kingdom.